The Astrophysical Journal, 891:137 (30pp), 2020 March 10 https://doi.org/10.3847/1538-4357/ab75ef

A Systematic Study of the Dust of Galactic Supernova Remnants. I. The Distance and the Extinction

He Zhao[1,2], Biwei Jiang[1], Jun Li[1], Bingqiu Chen[3], Bin Yu[1], and Ye Wang[1]
[1] Department of Astronomy, Beijing Normal University, Beijing 100875, People's Republic of China; bjiang@bnu.edu.cn
[2] University Côte d'Azur, Observatory of the Côte d'Azur, CNRS, Lagrange Laboratory, Observatory Bd, CS 34229, F-06304 Nice cedex 4, France; he.zhao@oca.eu
[3] South-Western Institute for Astronomy Research, Yunnan University, Kunming, Yunnan 650091, People's Republic of China
Received 2019 November 21; revised 2020 February 11; accepted 2020 February 11; published 2020 March 13

Abstract

By combining the photometric, spectroscopic, and astrometric information of the stars in the sightline of supernova remnants (SNRs), the distances to and the extinctions of 32 Galactic SNRs are investigated. The stellar atmospheric parameters are from the Sloan Digital Sky Survey−DR14/Apache Point Observatory Galaxy Evolution Experiment and Large sky Area Multi-Object fiber Spectroscopic Telescope−DR5/LEGUE spectroscopic surveys. The multiband photometry, from optical to infrared, are collected from the *Gaia*, APASS, Pan-STARRS1, Two Micron All Sky Survey, and *Wide-field Infrared Survey Explorer* surveys. With the calibrated *Gaia* distances of individual stars, the distances to 15 of 32 SNRs are well determined from their produced extinction and association with molecular clouds. The upper limits of distance are derived for three SNRs. The color excess ratios $E(g_{\rm P1}-\lambda)/E(g_{\rm P1}-r_{\rm P1})$ of 32 SNRs are calculated, and their variation with wavebands is fitted by a simple dust model. The inferred dust grain size distribution bifurcates: while the graphite grains have comparable size to the average interstellar medium dust, the silicate grains are generally larger. Along the way, the average extinction law from optical to near-infrared of the Milky Way is derived from the 1.3-million-star sample and found to agree with the CCM89 law with $R_{\rm V}=3.15$.

Unified Astronomy Thesaurus concepts: Extinction (505); Supernova remnants (1667); Interstellar dust (836)

1. Introduction

Supernovae (SNe) have profound effects on their environments as a violent process, by injecting kinetic energy on the order of 10^{51} erg into the interstellar medium (ISM). The high-speed expansion of the ejecta produces strong shocks that interact with the surrounding circumstellar and interstellar dust. This interaction destroys the ambient interstellar dust and alters the size of the dust grains (Lakićević et al. 2015). Whether the grains become smaller or bigger is not clear. On one hand, the energetic particles ($v > 150$ km s^{-1}) more often in fast shocks knock atoms off the grain surface (the so-called sputtering process, Dwek et al. 1996), which results in a deficit of small grains in supernova remnants (SNRs). On the other hand, the grain–grain collision dominant in slow shocks ($v \leqslant 50$–80 km s^{-1}) mainly destroys big grains, which results in a deficit of big grains (Jones et al. 1994). Nozawa et al. (2007) modeled the process of dust evolution in SNRs and found that the survival of dust in SNRs depends on the density of the ambient medium, e.g., in the case of 1 cm^{-3} typical of our ISM, small (<0.05 μm) grains are completely destroyed, intermediate (between 0.05 and 0.2 μm) grains are trapped into the dense shell, and big grains (>0.2 μm) are not changed significantly. The increase of the ambient density would shift the border size toward smaller grains. In addition to the initial size, the fate also depends on the composition of the dust. Nozawa et al. (2007) found that silicate dust may be more easily influenced than carbonaceous dust. Detection of SiO line emission in shocks is evidence of the destruction of silicate dust (Guillet et al. 2009). Thus, the shocks can modify the dust composition abundance in addition to the dust size distribution.

The changes in the dust size and component leave footprints in the dust emission from the SNRs. Andersen et al. (2011) analyzed the infrared (IR) spectral energy distribution (SED) and spectra of 14 Galactic SNRs and derived the ratio of very small grains to big grains. They found this ratio to be higher for most of their SNRs than that in the plane of the Milky Way, which may be explained by dust shattering that destroys big grains. Meanwhile, this ratio is lower than in the Galactic plane for two SNRs, indicating that sputtering is responsible to the dust destruction. Temim & Dwek (2013) modeled the SED with the *Herschel* far-infrared observation of the Crab Nebula and found a fairly large maximum grain size up to 0.1 μm or bigger, although Temim et al. (2012) argued for a small grain size of <0.05 μm from the dust emission measured by *Spitzer* at relatively short wavelengths. On the dust composition, Andersen et al. (2011) found that all 14 of their SNRs show evidence of polycyclic aromatic hydrocarbon emission, and silicate emission at 20 μm in two SNRs. Arendt et al. (1999) analyzed the *Infrared Space Observatory*/Short Wave Spectrometer spectrum of Cas A and identified an emission feature at ∼22 μm that could not be fitted by typical astronomical silicate. This is confirmed by the *Spitzer*/IRS observation in which Rho et al. (2008) detected a feature around 21 μm and which they explained by combining a few types of oxygen-bearing dust species.

Similar to the dust emission, the extinction by dust reveals the changes in the dust size distribution and composition of SNRs as well because the extinction law depends sensitively on the size and composition of the dust. As an experiment, Zhao et al. (2018, hereafter Paper I) studied the extinction and dust of the Monoceros SNR (G205.5+0.5). By taking the stars along the sightline of the SNR as tracers of the SNR extinction, Paper I derived the distance to the Mon SNR and the extinction produced by the SNR dust in the near-infrared (NIR) bands (namely the Two Micron All Sky Survey (2MASS) $JHK_{\rm S}$). The present work is an extension of Paper I, whose principles and methods are followed. Our goals include the estimation of distances to the SNRs and the study of their extinction law to

explore the effect of the SN explosion on both the SN ejecta and mainly the interstellar dust grains. First, the stars in the sightline toward the SNR are selected, and their interstellar extinctions are calculated. Second, the distance to the SNR is estimated from the position where the extinction increases sharply due to the higher dust density of the SNR than its foreground ISM. Last, the extinction law and the dust properties of the SNR are derived. It should be clarified that the dust of an SNR is merely produced by the SN ejecta. The dust produced by the SN ejecta is hardly more than a solar mass, which is shown for the case of young SNRs. For example, Matsuura et al. (2015) derived 0.8 $M_{\odot}$ for SN 1987A, Bevan et al. (2017) derived ∼1.1 $M_{\odot}$ for Cas A, and Owen & Barlow (2015) 0.6 $M_{\odot}$ for the Crab Nebula. However, the expansion of the SN shock waves can sweep up massive enough ambient interstellar dust to produce relatively large extinction jumps, in particular so considering that many SN explosions occur in large molecular clouds (MCs). Draine (2009) estimated the ISM mass to be swept by an SN explosion of about 1000 $M_{\odot}$. Compared to Paper I, we make a few important improvements: (1) the stellar distance is measured by *Gaia* and extracted from the newly released *Gaia* DR2 catalog. The distance from the *Gaia* parallax is a geometrical measurement without dependence on a stellar model and interstellar extinction; (2) the extinction curve is derived from the optical to IR, which reveals more accurately the properties of the SNR dust, whereas Paper I only studied the NIR extinction law that might be universal (Wang & Jiang 2014); and (3) the study is systematic by including many more SNRs, and the conclusion will be drawn from a wider range of SNRs.

The paper is organized as follows. In Section 2, we describe the data sets and objects used in this work and the quality control to build the star sample. The methods underpinning the determination of intrinsic color indices and extinctions are introduced in Section 3 in which an extinction-distance model to fit the reddening profile at a given line of sight is also described. The main results and discussions are presented in Section 4 and summarized in Section 5.

2. Data

We collect stellar parameters (effective temperature $T_{\rm eff}$, surface gravity log g, and metallicity [Fe/H]) from the Large sky Area Multi-Object fiber Spectroscopic Telescope (LAMOST) and Apache Point Observatory Galaxy Evolution Experiment (APOGEE) surveys, photometric data from the *Gaia*, Pan-STARRS1, AAVSO Photometric All-Sky Survey (APASS), 2MASS, and *Wide-field Infrared Survey Explorer* (*WISE*) surveys. The distance information is extracted from the *Gaia* parallax. After the quality control, each star in our sample has full information of stellar parameters, 11-band photometry from optical to IR, and distance.

2.1. LAMOST

LAMOST is a reflecting Schmidt telescope operated by the National Astronomical Observatories, Chinese Academy of Science. It can obtain 4000 spectra in a single exposure at the resolution $R = 1800$ with the wavelength coverage of 3700 Å $< \lambda <$ 9100 Å (Zhao et al. 2012; Deng 2014). LAMOST completed its fifth-year survey in July 2017, and the LAMOST–DR5 catalog contains over 9 million spectra. In this work, we make use of its catalog of over 5 million A-, F-, G-, and K-type stars for which the stellar parameters are highly reliable.[4]

2.2. APOGEE

APOGEE is a high-resolution ($R \approx 22{,}500$), *H*-band (1.51–1.70 μm) spectroscopic sky survey, providing accurate stellar parameters ($T_{\rm eff}$, log g, and [M/H]) for giant stars (Eisenstein et al. 2011). The newly released APOGEE data in Sloan Digital Sky Survey (SDSS)–DR14[5] (Abolfathi et al. 2018) includes both APOGEE-1 (SDSS-III) data and the first two years data from APOGEE-2 (SDSS-IV). The new data expand upon the previous APOGEE sample in both size (from ∼163,000 to over 270,000 stars) and spatial coverage (Majewski et al. 2016).

2.3. Pan-STARRS1

The Pan-STARRS1 3π survey was made with a 1.8 m telescope on Haleakala (Hodapp et al. 2004). The observations were conducted by using the 1.4 billion pixel GPC1 camera and performed in five broad filters: $g_{\rm P1}$, $r_{\rm P1}$, $i_{\rm P1}$, $z_{\rm P1}$, and $y_{\rm P1}$, with effective wavelengths of 4800 Å, 6200 Å, 7500 Å, 8700 Å, and 9600 Å, respectively (Onaka et al. 2008). The accuracy of relative and absolute photometry is better than 1% (Schlafly et al. 2012; Tonry et al. 2012). The $z_{\rm P1}$, and $y_{\rm P1}$ data are not used in our research because the APASS survey makes no observation in these bands for relatively bright stars.

2.4. APASS

The APASS is conducted in five filters: Johnson *B* and *V*, and Sloan g', r', i', and reliable photometry ranges from about 10.0 mag to 17.0 mag in *V*-band (Henden & Munari 2014). APASS is carried out to bridge the gap between the surveys, like Tycho–2 $B_T V_T$ survey (accurate at $<$ 10 mag) and SDSS (saturating at $<$ 14 mag; Henden & Munari 2014; Munari et al. 2014). The APASS−DR9 covered about 99% of the sky and contains over 60 million objects[6] (Henden et al. 2016). As the Pan-STARRS1 survey has a saturation problem with relatively bright stars, we use APASS survey, instead of Pan-STARRS1, to provide the photometries in *gri*-bands for stars brighter than 14.0, 14.4, and 14.4 mag in the $g_{\rm P1}$, $r_{\rm P1}$, and $i_{\rm P1}$ bands, respectively, following the criteria of Schlafly et al. (2016). To complete the transformation of photometric system from Pan-STARRS1 to SDSS, the quadratic relations by Tonry et al. (2012) are used.

2.5. 2MASS

The 2MASS provides the most widely used photometric data in the NIR bands: *J* (1.24 μm), *H* (1.66 μm), and $K_{\rm S}$ (2.16 μm) (Cohen et al. 2003). The completeness of 2MASS is over 99% for $J < 15.8$, $H < 15.1$, and $K_{\rm S} < 14.3$ mag, and the 2MASS point-source catalog we used in this work contains over 470 million objects (Cutri et al. 2003).

2.6. WISE

WISE is an IR space telescope with a diameter of 40 cm. It was launched in 2009 and performed a mid-IR full-sky survey

[4] See http://dr5.lamost.org/.
[5] See http://www.sdss.org/dr14/.
[6] See https://www.aavso.org/apass.

in four bands: W_1 (3.35 μm), W_2 (4.60 μm), W_3 (11.56 μm), and W_4 (22.09 μm; Wright et al. 2010). The AllWISE source catalog provides the photometric data. We only take the W_1 and W_2 bands into use because the sensitivities of the long-wavelength bands W_3 and W_4 are significantly lower and unable to match the sensitivities of the other bands.

2.7. Gaia

The newly released *Gaia* DR2 contains 1.3 billion sources with trigonometirc parallaxes, three bands photometry (G_{BP}, G, G_{RP}), and proper motions (Gaia Collaboration et al. 2018). The central wavelengths of G_{BP}, G, and G_{RP} are 532, 673, and 797 nm, respectively (Jordi et al. 2010). The distances used in our work are derived from the *Gaia* parallaxes and calibrated by Bailer-Jones et al. (2018).

2.8. Data Combination and Quality Control

With these many data sets in use, we first combine the LAMOST and APOGEE catalogs, where the stellar parameters from APOGEE are kept for their higher precision for the overlapping sources, although these two sets of stellar parameters are generally consistent within the error range (Anguiano et al. 2018). Then the stars with stellar parameters from the spectroscopic surveys are cross-matched with the multiband photometric data from *Gaia*, Pan-STARRS1, APASS, 2MASS, and *WISE*, as well as *Gaia* distances. All of the catalogs are cross-matched within 1″.

The measurements of stellar parameter, photometric magnitude, and parallax are required to fulfill the following requirements in order to obtain reliable results:

1. The photometric error in all bands is smaller than 0.1 mag.
2. The errors of stellar effective temperature and surface gravity are $\sigma_{T_{\rm eff}} < 150$ K, $\sigma_{\log g} < 0.2$ dex, respectively.
3. Sources from LAMOST should have SNR $g > 30$ (signal-to-noise ratio in the g-band), and sources from APOGEE should have S/N > 100 and VSCATTER $< 0.3\,{\rm km\,s^{-1}}$ (the velocity scattering of multi-epoch measurements) to exclude binary stars.
4. The fractional error of stellar distance from *Gaia* DR2 is smaller than 30%, and the sources with failed calibration are excluded.

Furthermore, the dwarfs and giants are judged according to the following criteria:

1. Dwarfs: $\log g > 4$ for 4000 K $< T_{\rm eff} <$ 6500 K; $\log g >$ 3.5 for 6500 K $< T_{\rm eff} <$ 8500 K.
2. Giants: 3900 K $< T_{\rm eff} <$ 5400 K, $1 < \log g < 3$.
3. For both dwarfs and giants, $-1.0 <$ [Fe/H] < 0.5 is required because the measured metallicity has large uncertainty outside this range.

The latest data sets extend significantly the ranges of stellar parameters for both dwarfs and giants in comparison with the star sample used in Paper I. Finally, 1,115,536 dwarfs and 221,820 giants are selected to constitute our star sample, all with stellar parameters, *Gaia* distance, and 11-band photometries: g_{P1}, G_{BP}, r_{P1}, G, i_{P1}, G_{RP}, J, H, K_S, W_1, W_2. Stars can be as faint as $g_{P1} = 20$ mag and trace the dust with $E(g_{P1} - K_S) \approx 14.0$ mag. Meanwhile, their distances can reach the zone farther than 15 kpc, though mostly within 6 kpc. These characteristics make it possible to detect Galactic SNRs in an extensive range, and perform a systematic study of their distances and extinction laws.

3. Method

3.1. Intrinsic Color Indices: From Optical to IR

The "blue-edge" method is widely used to derive the stellar intrinsic color index from the effective temperature $T_{\rm eff}$ for a given luminosity class (see Ducati et al. 2001; Wang & Jiang 2014; Xue et al. 2016; Jian et al. 2017). The premise is that the extinction-free stars constitute the blue edge in the $T_{\rm eff} - C_{\lambda_1\lambda_2}$ (observed color) diagram for large stellar surveys, because they have the smallest observed colors that are indeed their intrinsic colors at the given $T_{\rm eff}$. By deriving the analytic function of this blue edge, the stellar intrinsic color can then be calculated from its effective temperature. In practice, the median color of some fraction of the bluest stars is taken as the intrinsic color instead of choosing the exact bluest one, because the photometric and parameter's uncertainties would shift the colors in some range. Jian et al. (2017) found that 10% is an appropriate fraction for the sources with photometric errors around 0.05 mag, i.e., the median color of the bluest 10% of stars can represent the intrinsic color for each assigned temperature interval. In comparison with the NIR bands, metallicity has a heavier influence on intrinsic colors in the optical bands involved in the present work. So, the star sample is further divided into six groups with a step of 0.25 dex in the measured [Fe/H] from -1 to 0.5. With this subdivision, the sample stars for $g_{P1} - G_{BP}$ and $g_{P1} - G$ with $-1 <$ [Fe/H] < -0.75 are not adequate in number, and the bluest 20% rather than bluest 10% of stars are chosen. The comparison between different [Fe/H] groups finds that the intrinsic colors of dwarfs are hardly affected by metallicity. Meanwhile, giant stars show a systematic change with [Fe/H], i.e., their intrinsic colors increase with [Fe/H].

An exponential function is fitted to the relations between the intrinsic colors and $T_{\rm eff}$ in each group:

$$C^0_{\lambda_1\lambda_2} = A_0 \exp\left(-\frac{T_{\rm eff}}{A_1}\right) + A_2. \quad (1)$$

For the 11 photometric bands, 10 intrinsic color indices are derived with g_{P1} as the reference band, namely $(g_{P1} - G_{BP})_0$, $(g_{P1} - r_{P1})_0$, $(g_{P1} - G)_0$, $(g_{P1} - i_{P1})_0$, $(g_{P1} - G_{RP})_0$, $(g_{P1} - J)_0$, $(g_{P1} - H)_0$, $(g_{P1} - K_S)_0$, $(g_{P1} - W_1)_0$, and $(g_{P1} - W_2)_0$ for each metallicity group and for dwarfs and giants, respectively. The coefficients are presented in Table 1. The case of the color index, $(g_{P1} - K_S)_0$ is shown as an example in Figure 1, as well as the comparison of different [Fe/H] groups.

As discussed in Paper I, the uncertainty brought by the fitting technique is on the order of several thousandths of a magnitude. The error induced by the adopted bluest fraction is 0.03 mag for dwarfs and 0.06 mag for giants (Jian et al. 2017). Since we further divided the sample according to [Fe/H], the influence of [Fe/H] is reduced in comparison with Paper I. In conclusion, the total uncertainty of the calculated intrinsic color is comparable to the photometric error ($\sim$0.05 mag) for most of the sample stars.

Table 1
Fitting Coefficients of Intrinsic Color Indices to Equation (1)

	[Fe/H]	[−1.00, −0.75]			(−0.75, −0.50]			(−0.50, −0.25]		
	Coefficients	A_0	A_1	A_2	A_0	A_1	A_2	A_0	A_1	A_2
Dwarf	$(g_{P1}-G_{BP})_0$	3.3965	1642.0	−0.1198	4.8156	1337.7	−0.1111	18.336	948.82	−0.0994
	$(g_{P1}-r_{P1})_0$	6.8456	2387.4	−0.3220	8.1132	2044.1	−0.1799	8.2938	2042.0	−0.1735
	$(g_{P1}-G)_0$	10.124	1722.8	−0.0682	8.0118	1826.3	−0.0766	10.617	1629.8	−0.0443
	$(g_{P1}-i_{P1})_0$	9.8239	2481.3	−0.5425	10.521	2284.1	−0.4120	10.533	2295.4	−0.4007
	$(g_{P1}-G_{RP})_0$	10.762	2307.3	−0.1377	11.827	2094.8	−0.0008	10.509	2289.4	−0.0728
	$(g_{P1}-J)_0$	15.609	2457.1	−0.2175	15.855	2345.0	−0.0679	15.086	2445.1	−0.1121
	$(g_{P1}-H)_0$	18.059	2626.9	−0.4107	17.568	2624.1	−0.3438	18.543	2486.5	−0.1971
	$(g_{P1}-K_S)_0$	20.174	2469.5	−0.3111	18.812	2563.9	−0.3301	19.969	2408.4	−0.1413
	$(g_{P1}-W_1)_0$	20.587	2452.3	−0.2629	22.085	2261.9	−0.0259	20.018	2428.3	−0.1260
	$(g_{P1}-W_2)_0$	21.872	2354.5	−0.2384	22.734	2204.9	−0.0059	19.799	2428.9	−0.1472
Giant	$(g_{P1}-G_{BP})_0$	13604.	367.94	−0.0337	37.086	784.62	−0.0772	50.532	729.79	−0.0521
	$(g_{P1}-r_{P1})_0$	56.716	952.14	0.1888	17.020	1349.3	0.0955	45.508	935.24	0.3492
	$(g_{P1}-G)_0$	148.83	766.59	0.2257	47.262	875.52	0.1895	94.287	809.30	0.3126
	$(g_{P1}-i_{P1})_0$	110.00	893.97	0.3185	48.245	1090.4	0.2713	126.49	817.69	0.5517
	$(g_{P1}-G_{RP})_0$	81.359	967.65	0.5911	54.792	1055.3	0.6085	93.782	887.04	0.8110
	$(g_{P1}-J)_0$	136.32	957.51	1.0640	33.534	1543.2	0.5248	85.929	1030.1	1.2573
	$(g_{P1}-H)_0$	151.16	994.32	1.2691	43.596	1507.3	0.7381	57.385	1283.2	1.2327
	$(g_{P1}-K_S)_0$	183.70	952.47	1.3871	48.655	1472.0	0.7715	73.571	1193.4	1.3819
	$(g_{P1}-W_1)_0$	169.17	977.48	1.4094	45.457	1528.7	0.7448	111.16	1044.6	1.6544
	$(g_{P1}-W_2)_0$	168.39	969.26	1.3938	46.887	1475.8	0.8206	110.03	1030.2	1.6545
	[Fe/H]	(−0.25, 0]			(0, 0.25]			(0.25, 0.50]		
	Coefficients	A_0	A_1	A_2	A_0	A_1	A_2	A_0	A_1	A_2
Dwarf	$(g_{P1}-G_{BP})_0$	20.971	931.52	−0.1084	19.110	966.03	−0.1204	17.835	949.16	−0.1151
	$(g_{P1}-r_{P1})_0$	7.4441	2213.3	−0.2120	6.8197	2350.9	−0.2362	6.1199	2485.9	−0.2428
	$(g_{P1}-G)_0$	11.585	1605.0	−0.0505	12.553	1574.5	−0.0517	8.4923	1803.1	−0.0690
	$(g_{P1}-i_{P1})_0$	9.8520	2446.6	−0.4581	9.0829	2608.5	−0.5086	8.1627	2775.8	−0.5330
	$(g_{P1}-G_{RP})_0$	9.8195	2443.9	−0.1390	9.4192	2522.7	−0.1604	7.6727	2872.5	−0.2283
	$(g_{P1}-J)_0$	13.924	2653.2	−0.2475	12.894	2842.6	−0.3504	11.733	2990.6	−0.3670
	$(g_{P1}-H)_0$	16.722	2753.7	−0.4145	15.973	2852.3	−0.4735	14.814	2950.7	−0.4802
	$(g_{P1}-K_S)_0$	18.026	2655.7	−0.3501	16.813	2812.7	−0.4547	15.780	2859.3	−0.4125
	$(g_{P1}-W_1)_0$	18.272	2643.9	−0.3003	16.936	2814.9	−0.4122	16.338	2813.1	−0.3521
	$(g_{P1}-W_2)_0$	17.817	2663.2	−0.3203	16.283	2866.8	−0.4480	15.557	2879.8	−0.3922
Giant	$(g_{P1}-G_{BP})_0$	357.66	532.77	−0.0141	15.649	1004.2	−0.1105	1866.1	437.57	0.0190
	$(g_{P1}-r_{P1})_0$	61.869	864.50	0.4104	96.074	779.73	0.4665	145.14	706.00	0.5516
	$(g_{P1}-G)_0$	248.56	652.00	0.4096	211.79	688.79	0.4016	297.70	643.10	0.4728
	$(g_{P1}-i_{P1})_0$	234.13	720.31	0.6417	558.47	615.34	0.7310	1329.6	538.96	0.8152
	$(g_{P1}-G_{RP})_0$	198.68	750.36	0.9311	346.95	672.96	1.0061	1730.7	519.88	1.1741
	$(g_{P1}-J)_0$	255.12	782.73	1.5623	507.36	680.09	1.7068	1503.2	564.41	1.9059
	$(g_{P1}-H)_0$	172.74	903.35	1.7851	500.71	706.91	2.0963	882.81	633.18	2.2639
	$(g_{P1}-K_S)_0$	209.43	873.48	1.8894	685.39	674.28	2.2283	1157.1	610.78	2.3963
	$(g_{P1}-W_1)_0$	291.84	810.53	2.0519	947.96	638.52	2.3613	959.31	636.16	2.4246
	$(g_{P1}-W_2)_0$	307.48	791.57	2.0310	1012.8	624.43	2.3192	774.61	654.21	2.3124

3.2. The Extinction-distance Model

With the intrinsic color indices of individual stars derived from the blue-edge method, their color excesses are calculated straightforwardly by subtracting the intrinsic colors from the observed. Then, the variation of reddening along distance toward a given line of sight can be obtained with the help of *Gaia* distance of individual stars. In order to determine the distance to an SNR, the extinction-distance model used in Chen et al. (2017) is adopted because this model is insensitive to the outliers:

$$A(d) = A^0(d) + A^1(d), \tag{2}$$

where $A(d)$ is the total extinction measured along the sightline. $A^1(d)$ is the contribution from the dust in the SNR. Assuming that the integrated extinction is dominated by one SNR cloud, $A^1(d)$ can be described by the function

$$A^1(d) = \frac{\delta A}{2} \times \left[1 + \mathrm{erf}\left(\frac{x - d_0}{\sqrt{2}\ \delta d}\right)\right] \tag{3}$$

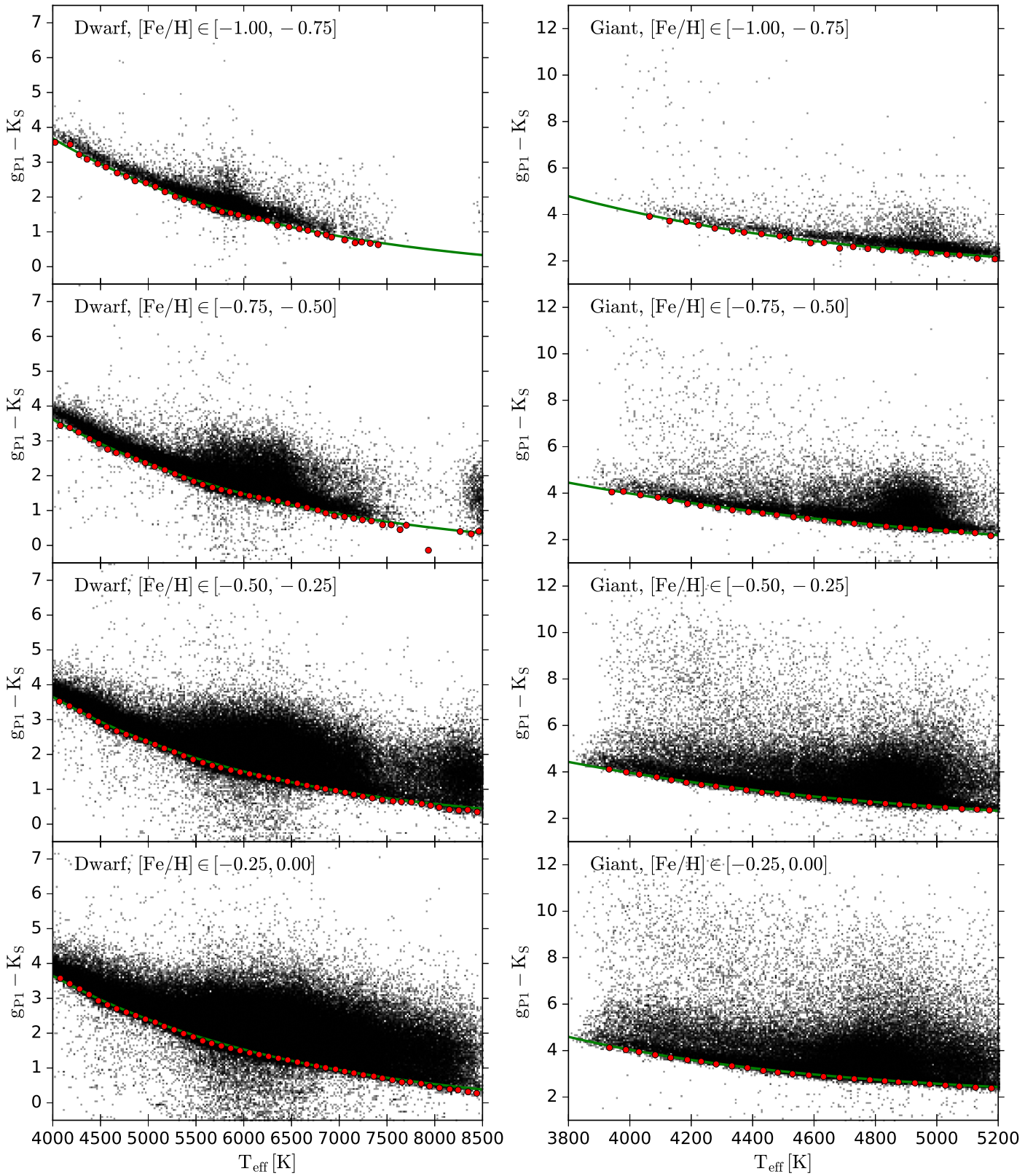

Figure 1. Determination of the intrinsic color index $(g_{P1} - K_S)_0$ with T_{eff} for both dwarfs (left panels) and giants (right panels) in different [Fe/H] groups. The red dots denote the intrinsic colors derived in each T_{eff} bin, and the green lines represent the fitting curves. The luminosity class and [Fe/H] group are indicated in the top left corner on each panel. The last two panels compare $(g_{P1} - K_S)_0$ derived for different [Fe/H] group for both dwarf (left panel) and giant (right panel).

where δA represents the amplitude of the extinction jump, i.e., the extinction of the SNR, d_0 is the distance to the center of the SNR and δd is the width of the SNR calculated from the angular diameter and d_0 of the SNR.

$A^0(d)$ represents the extinction provided by the diffuse interstellar dust. Chen et al. (2017) suggested a two-order polynomial to describe $A^0(d)$, which is reasonable for the nearby zone, but the integrated reddening will drop quickly

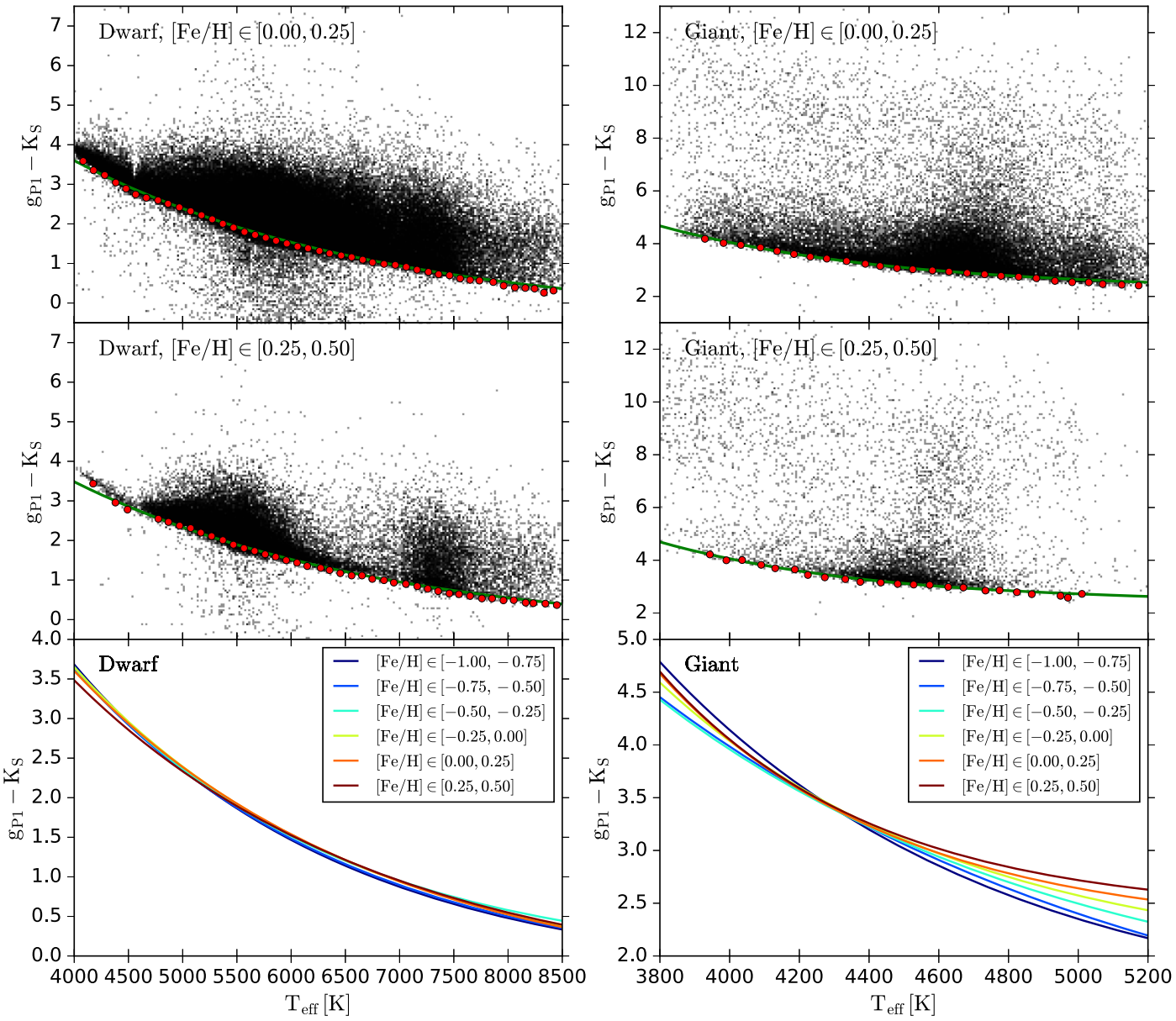

Figure 1. (Continued.)

with distance at large. To avoid this unreasonable tendency, we replace the quadratic term with a square root,

$$A^0(d) = a \times d + b \times \sqrt{d}, \quad (4)$$

where a and b are the fitting coefficients. It should be kept in mind that how the interstellar reddening changes with distance is still not clear and needs further investigation. Here, we only present a mathematical fitting to the foreground and background extinction.

A Markov Chain Monte Carlo (MCMC) procedure (Foreman-Mackey et al. 2013) is performed to optimize the free parameters in the model. We apply a scheme similar to Kos (2017) to make the procedure more stable. A first Markov chain with 100 walkers and 200 steps is run to estimate the initial parameters for the final chain. Then 1000 steps with 128 walkers are run, and the last 750 steps from each walker are used to sample the final posterior. The median values (50th percentile) of the posterior distribution are taken as the best estimates, with uncertainties derived from the 16th and 84th percentile values. If the parameters tend to gather into two distinct groups during the MCMC sampling, a new distance component is added to the model, which means there are two distances for one sightline. Six SNRs are assigned with a second distance component.

The distance to the Rosette Nebula (a well-studied H II region) is fitted as a test of the model. Paper I determined its distance to be 1.55 kpc, which coincides with literature results. Two-hundred ninety-eight dwarfs and 43 giants are selected from our star sample toward the region of the Rosette Nebula defined by Paper I. The fitting results are shown in Figure 2 for all 10 color excesses. The derived distances from different bands are highly consistent with each other with a standard deviation of 0.06 kpc. Their mean value, 1.58 kpc, agrees very well with previous works. Figure 3 is the corner plot of the parameters at $E(g_{P1} - K_S)$, which shows all of the one- and two-dimensional projections of the posterior distributions of the parameters. The blue squares and lines demonstrate the

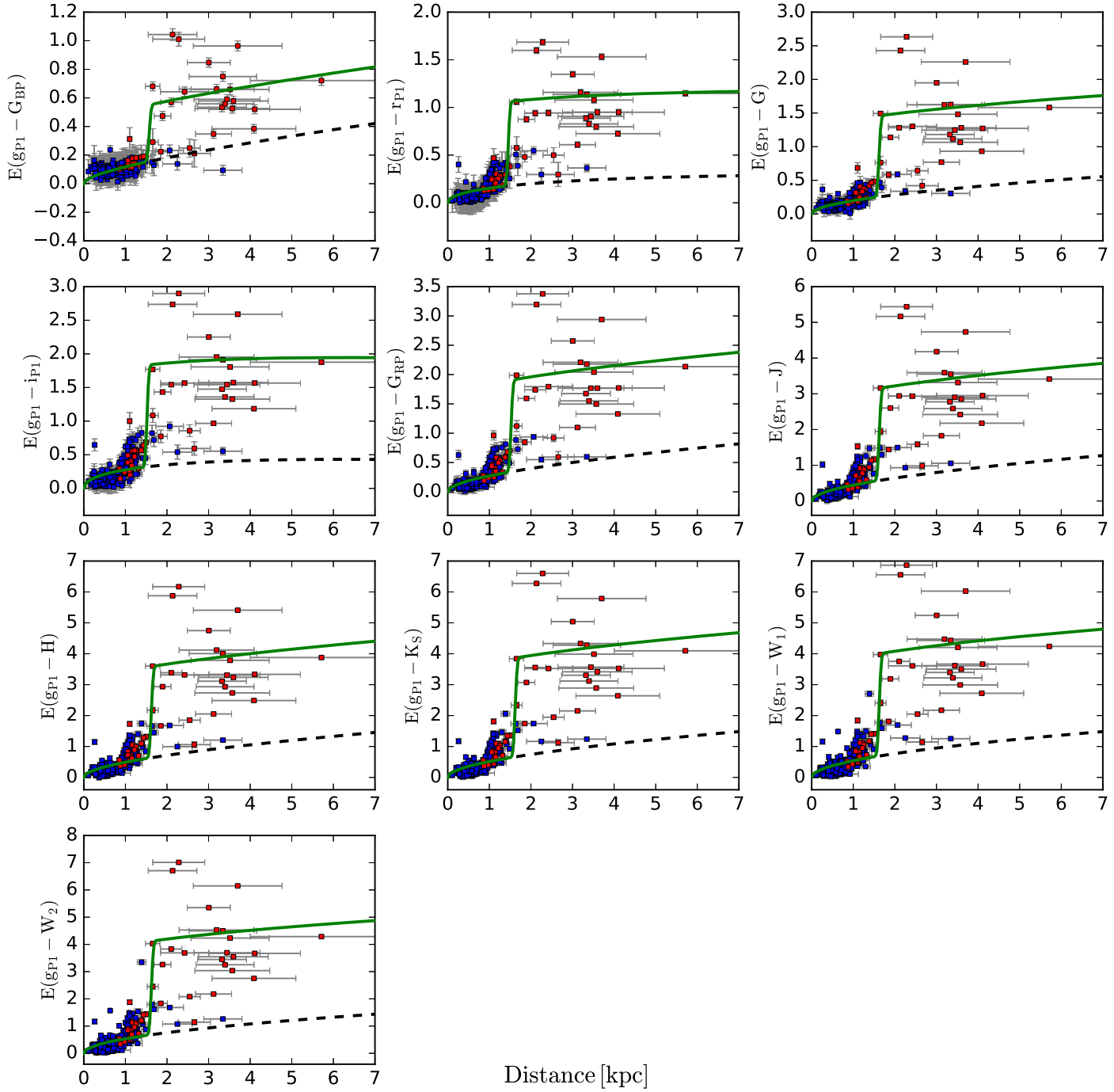

Figure 2. The fitting result of the extinction-distance model (Equations (2)–(4)) to the Rosette Nebula in the 10 color excesses. The blue and red squares are dwarf and giant stars, respectively. The gray lines represent the error bars. The green lines are the best-fitting curves. The black dashed line is the ISM component derived from the extinction-distance model.

best-fit values of the parameters, which also exhibit the order of the uncertainties of the fitted parameters.

3.3. Foreground Extinction

To measure the extinction produced by the SNR alone, foreground extinction must be extracted. In Equation (2), the foreground extinction is described by $A^0(d)$ (Equation (4)). In the case that the observed data can be well fitted by Equation (2), the foreground extinction can be determined simultaneously with the extinction of the SNR (δA). Unfortunately, some cases cannot be well fitted by Equation (2) mostly because the sample stars are inadequate in number either due to the small region of the SNR or the incomplete observation. In such a case, we have to select a model for foreground interstellar extinction. We choose a typical diffuse sightline to represent the common extinction-distance model of ISM to simplify the calculation, although the extinction-distance model should change with sightlines. This may introduce additional errors in estimating the

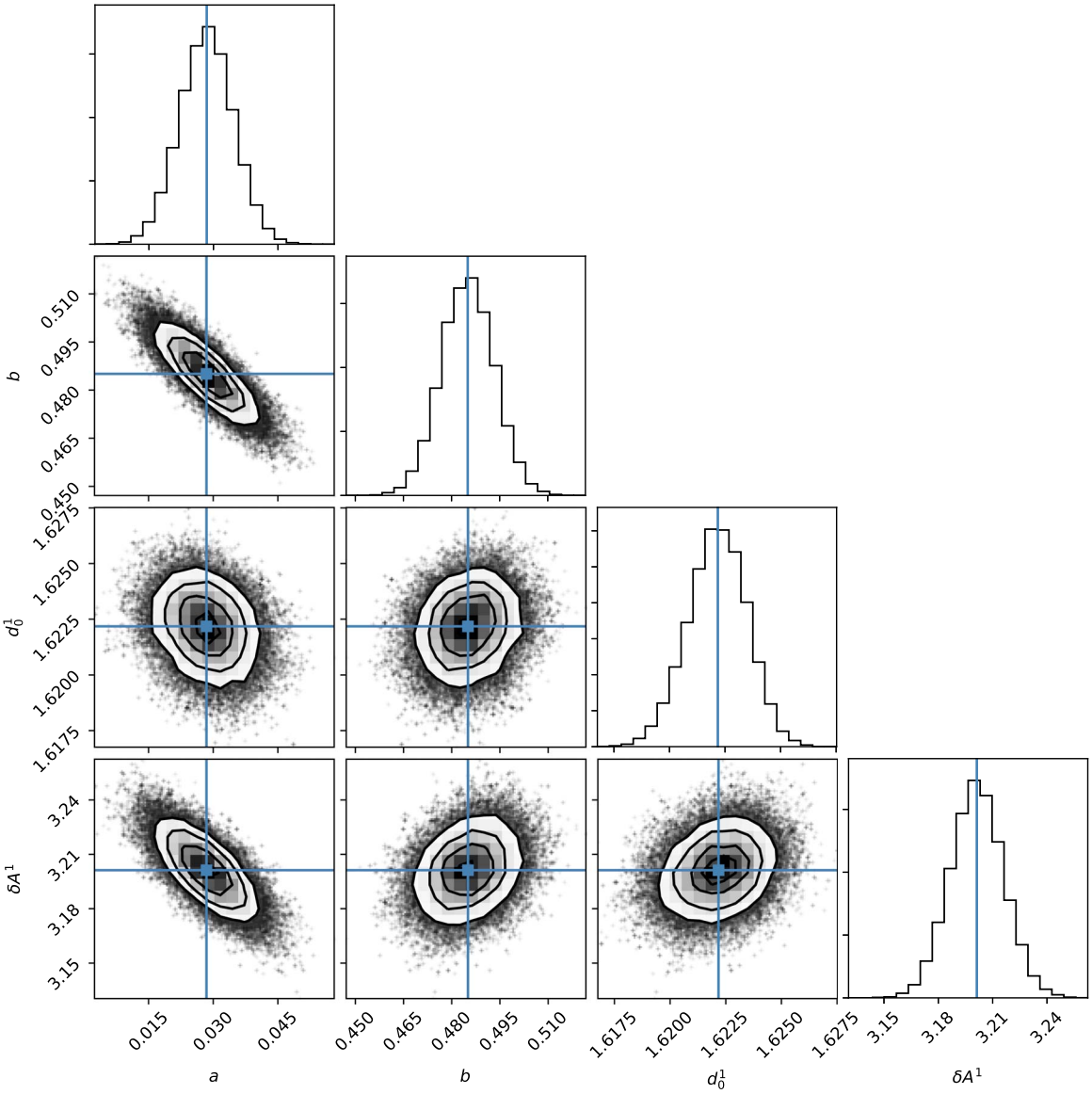

Figure 3. The corner plot of the fitting to the Rosette Nebula in $E(g_{\rm P1} - K_{\rm S})$. The histograms show the distributions of the parameters. The contours present the covariances between each of them. The blue squares and lines indicate the best-fit values of the parameters.

extinction of these SNRs, but it has little influence on the distance determination.

Wang et al. (2017) reported a very diffuse region centered at ($l = 165.^\circ0$, $b = 0.^\circ0$, hereafter named "*l*165") based on the Milky Way's CO emission map (Dame et al. 2001). With a square region of $2^\circ \times 2^\circ$ toward "*l*165," 320 stars are picked from our star sample. Although this region was proven to be diffuse, the increase of extinction with distance still becomes steeper beyond 3 kpc as seen in Figure 4, which is caused by the Perseus arm. We have to apply the extinction-distance model (Equation (2)) to "*l*165," which resulted in both the ISM extinction and the extinction produced by the Perseus arm around 3.5 kpc. The derived ISM component is then used to represent the foreground extinction for the SNRs whose reddening profiles are not well fitted by the model Equation (2).

3.4. The SNR Region

The projected region for every SNR needs to be defined carefully to choose appropriate sample stars because the SNR morphology is usually irregular. The centers and angular sizes reported in the revised catalog of 294 Galactic SNRs by Green (2019) provide a very good initial estimation of the regions (the referred regions). We take a simple circle with the major radius from this catalog as the referred regions. The regions are further refined according to the radio observations of the SNRs.

The radio data are mostly taken from the Effelsberg 100 m telescope observation (Reich et al. 1990, 1997). The images of G74.0−8.5, G82.2+5.3, and G89.0+4.7 come from the Effelsberg Medium Latitude Survey at 1.4 GHz (Uyaniker et al. 1999). Some objects lack the Effelsberg observation and alternative data are taken. For G156.2+5.7, G178.2–4.2, and G182.4+4.3, the observations are made by the Urumqi 25 m telescope at 6 cm (Gao et al. 2010). The data of G65.3+5.7 and G70.0–21.5 are from the 4850 MHz GB6S survey (Condon et al. 1991, 1994). For G159.6+7.3, the 325 MHz observation from the Westerbork Northern Sky Survey (WENSS; Rengelink et al. 1997) is used.

For G65.1+0.6 and G108.2−0.6, only giant stars in the selected regions are available. We doubled the size of the regions

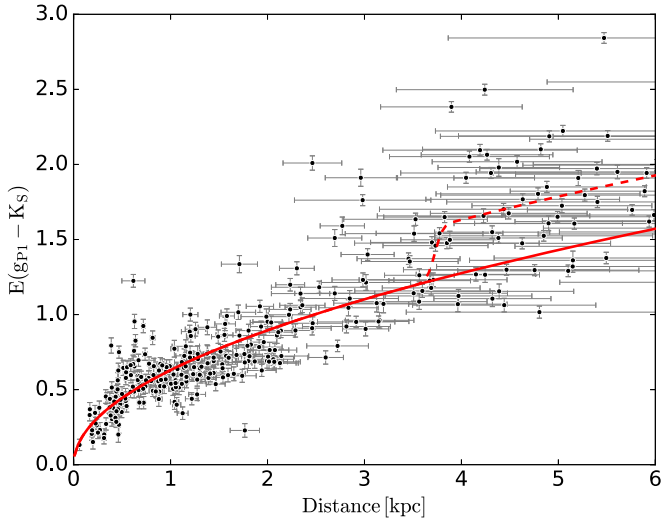

Figure 4. The run of reddening toward "*l*165," the common reference region, in $E(g_{\rm P1} - K_S)$. The black dots with error bars are the sample stars. The solid red line is the best fitted reddening profile, and the dashed red line is used to describe the extinction jump caused by the Perseus arm.

to enclose some foreground dwarf stars to determine the foreground extinction. The neighboring intensive radio sources blur the borders of G67.6+0.9, G108.2−0.6, G152.4−2.1, and G213.0−0.6. G65.3+5.7, G70.0−21.5, and G159.6+7.3 are very faint and large SNRs. The radiation field of some SNRs, e.g., G109.1−1.0, G119.5+10.2, and G189.1+3.0, extend beyond the referred regions, so larger polygonal fields are applied. If an SNR cannot be distinguished from its radio observation, the referred region is applied. The projected region of G205.5+00.5 (Monoceros) is from Paper I.

With the defined regions, we complete the source selection toward the sightlines of SNRs from our star sample. For 45 SNRs, there are dwarf and/or giant stars from our selected sample. But some SNRs in the Galactic center direction have too few stars in the sightline, and they are excluded since no reliable results can be derived. Finally, 32 SNRs are selected to study their distances and extinctions. The results are presented in Figure 5, along with the SNR regions and radio observations. To make the figures concise, we omit their contour lines and color bars. Different figures are in different intensity scales. It should be noted that the applied irregular regions prefer to follow some level of the contour lines enclosing the SNRs.

4. Results and Discussions

4.1. The SNR Distance

There are 32 Galactic SNRs in total covered by our star sample. We obtain reddening profiles for 21 of them by our extinction-distance model. Their distances are calculated by taking the average of the fitted distances from the reddenings of five IR bands relative to $g_{\rm P1}$, i.e., $g_{\rm P1} - J$, $g_{\rm P1} - H$, $g_{\rm P1} - K_S$, $g_{\rm P1} - W_1$, and $g_{\rm P1} - W_2$. The visual bands are dropped because their much smaller color excess relative to $g_{\rm P1}$, $E(g_{\rm P1} - \lambda)$, will introduce significant uncertainties. Meanwhile, the dispersion of distance from different bands is taken into account for estimating the final uncertainty together with the error provided by the MCMC procedure. In addition to these 21 SNRs, the distance of G78.2+2.1 can be reliably recognized by the conspicuous extinction jump, although the extinction-distance model cannot fit its reddening profile because of the absence of distant tracers. For other SNRs, the analysis yields upper limits or null results of distance. Seven of them have only giant stars as the distance and extinction tracers so that the background extinction cannot be determined. Consequently, no accurate distance is determined; instead, the upper limit is constrained by comparing the extinction of tracers with the reddening profile of "*l*165." The run of reddenings traced by our star sample toward every SNR plus the "*l*165" are shown in Figure 6, and their distances are presented in Tables 2–4, as well as the results from the literatures. It should be noted that the distances indicated in the figures may be slightly different from those reported in the tables because we only present the fitting results at $E(g_{\rm P1} - K_S)$ in Figure 6 while Tables 2–4 results from the average distance from five bands.

The 32 SNRs are classified into three levels according to the credibilities of the results. Level A includes 15 SNRs with well-determined distance. Because the SNRs are all located in the Galactic plane full of MCs, the detected extinction jump can plausibly be caused by the MCs in the sightline. However, since the core-collapse SN originates from massive stars, these SNRs are expected to associate with MCs. Then, the distance of such an SNR should agree with that of the associated MC. This argument is supported by the work of Yu et al. (2019), which takes the distance to the MC at the sightline as that of the SNR. Therefore, we searched for the SNRs in our sample that were previously suggested to be associated with MCs. It is found that nine of them have been verified to be associated with MCs by Jiang et al. (2010) and the references therein, namely G78.2+2.1, G89.0+4.7, G94.0+1.0, G109.1−1.0, G166.0+4.3, G189.1+3.0, G190.9−2.2, G205.5+0.5, and G213.0−0.6. In addition, G152.4−2.1, G160.9+2.6 and G182.4+4.3 are suggested to have associated MCs by Yu et al. (2019). Thus, these SNRs are more likely to sweep up massive amounts of dust of the ambient MC that can cause apparent extinction jump along the sightline. One more support comes from the reddening profiles derived from Green et al. (2019), which show no other apparent extinction jumps within 7 kpc toward these SNRs (see Figure 7), i.e., no confusing jump exists. Therefore, the distances to these 12 SNRs are regarded as well determined. G93.7−0.2, G156.2+5.7, and G206.9+2.3 are also classified as Level A because of their apparent extinction hikes and their dust properties are consistent with the expectation from SNRs (see Section 4.2.2).

The measurements of seven SNRs in Level B have lower credibilities. Their distances are either upper limits or less restricted. Both G82.2+5.3 and G108.2–0.6 exhibit apparent extinction jump, but they are still classified as Level B because no associated MC has been reported up to now, and the detected extinction jump may be caused by the foreground or background MC. However, there is still a high possibility that the distance is correct with further investigation of the association of the SNR and MC. For these sources, reliable upper limits of distance are determined for G74.0–8.5, G113.0+0.2, and G127.1+0.5, while not enough tracers are available toward G65.3+5.7 and G116.9+0.2 to well constrain the fittings. Level C contains five estimates with great uncertainties and five failed cases. Among them, the explorations to G179.0+2.6 and G180.0–1.7 are suggested to only detect some foreground clouds. Detailed discussions for individual cases are presented in the Appendix. The following discussions concentrate mainly on 22 SNRs in Level A (15) and B (7).

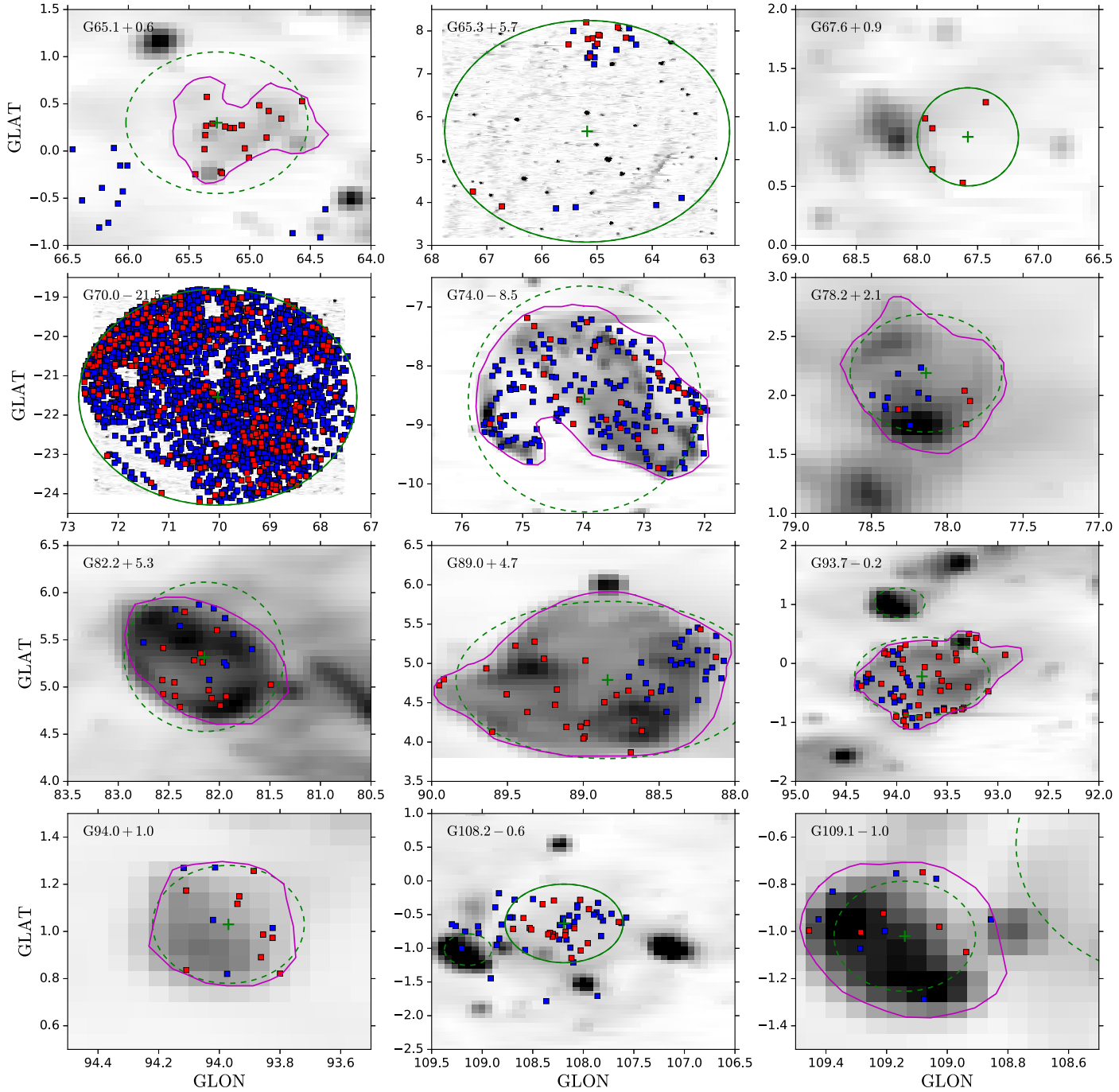

Figure 5. The selected stars and the SNR regions. The background gray image is the radio map. The green dashed circles represent the reference regions of SNRs from Green (2019), with green crosses indicating the centers. If the referred regions are used, they will be in solid lines. The magenta solid lines are manually defined regions, which follow some contour lines enclosing the SNRs. The blue and red squares denote the dwarfs and giants, respectively. All of the subpanels are in Galactic coordinates.

4.1.1. Comparison with the Distances from Two Dust Maps

The reddenings of SNRs can also be inferred from three-dimensional (3D) dust maps. Based on a recently released 3D dust map of Chen et al. (2019), Yu et al. (2019) analyzed the dust mappings of 12 SNRs toward the Galactic anticenter. Although they claimed reliable determination for only four sources, the distance is successfully determined for seven SNRs, namely G152.4–2.1, G160.9+2.6, G182.4+4.3, G189.1 +3.0, G190.9–2.2, G205.5+0.5, and G213.0–0.6. All of their results (presented in bold face in Table 2) are highly consistent with ours, which enhances the reliability of both results. This consistency is remarkable. Basically, Yu et al. (2019) determined the distance of the MC overlapping with the SNR in the radio image, which can be the distance of the SNR only if the SNR and the MC are interacting. Meanwhile, we determined the distance of the SNR according to the stars in the sightline of the SNR other than the stars to the neighboring MC. The agreement between the two distances implies that the SNR and the MC are interacting for the seven cases. On the other hand, Yu et al. (2019) did not find any associated MCs for the five other SNRs, and thus, no distance was determined.

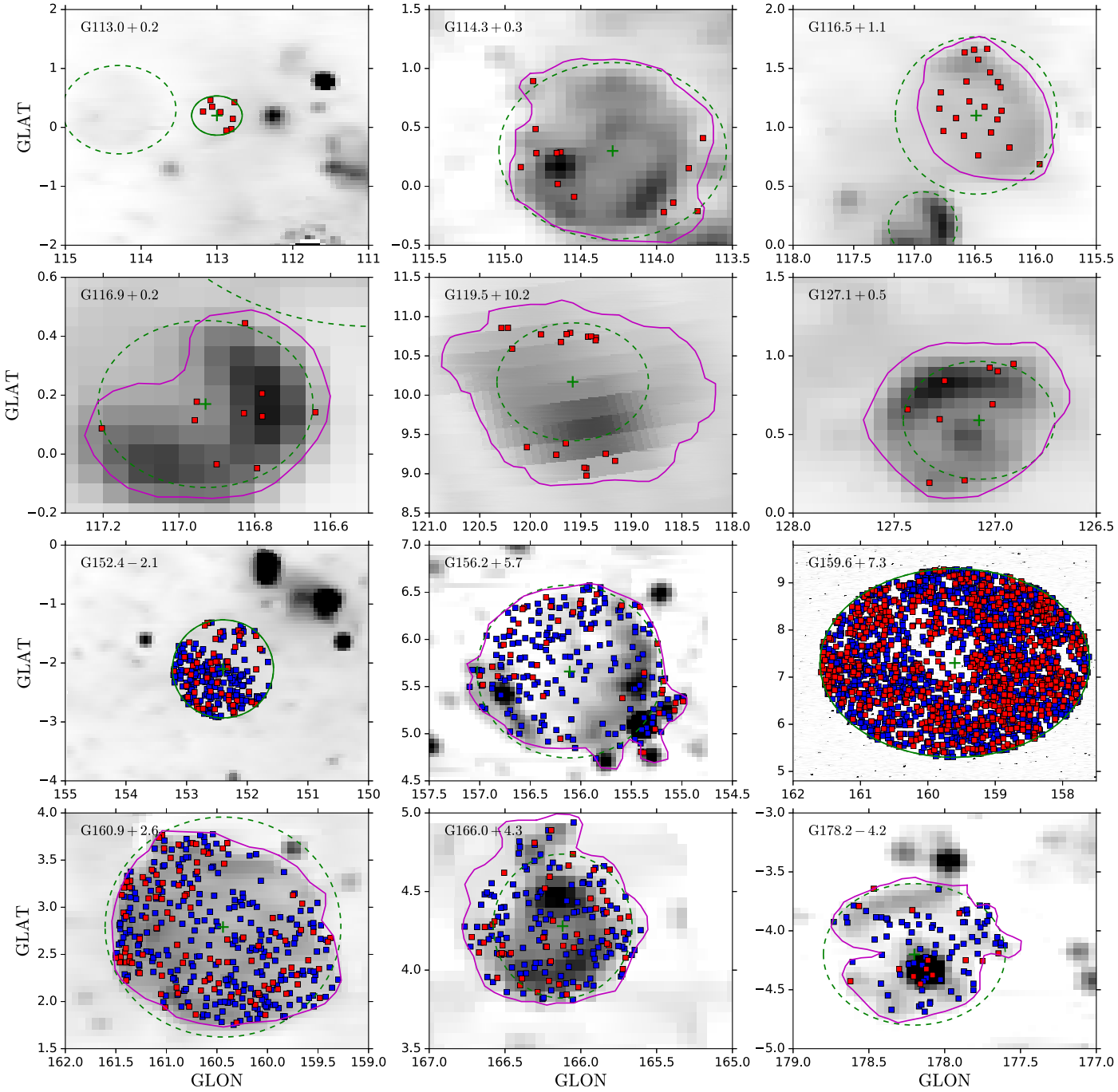

Figure 5. (Continued.)

Although massive stars are expected to be associated with MCs, many OB stars are field stars and some SNRs may be unassociated with any MC. In addition, the SNRs from type Ia SN usually have no association with MCs.

Green et al. (2019) constructed a 3D map of the Milky Way dust reddening with 800 million stars observed by Pan-STARRS1, 2MASS, and *Gaia*. The typical angular resolution of the map is from 3.′4 to 13.′7, and the distance ranges from 63 pc to 63 kpc. To retrieve a representative reddening profile from the Green et al. (2019) map for each of the 32 SNRs as well as the Rosette Nebula, we select the sightline of the measured high-extinction region within the SNR, and sample the dust map from 100 pc to 7 kpc with a step of 100 pc. It is noted that for Monoceros SNR, the sightline to an MC centered at ($l = 204.^{\circ}107$, $b = 0.^{\circ}471$) reported by Su et al. (2017) is applied. Our results are compared with this reddening map in Figure 7, where the fluctuation of the reddening profile is caused by the uncertainty of the dust map. High consistency is achieved for most of the SNRs in Level A, see, e.g., G78.2+2.1 and G190.9–2.2. In a few cases, like G89.0+4.7, no apparent extinction jump is present in the Green et al. (2019) map, which may be due to the relatively low spatial resolution of the Green et al. (2019) map that smoothed out the feature. For SNRs G82.2+5.3 and G108.2–0.6, there are additional jumps from the dust map besides the one revealed by our analysis with one distance component. The sharp increase at ∼0.3 kpc and the

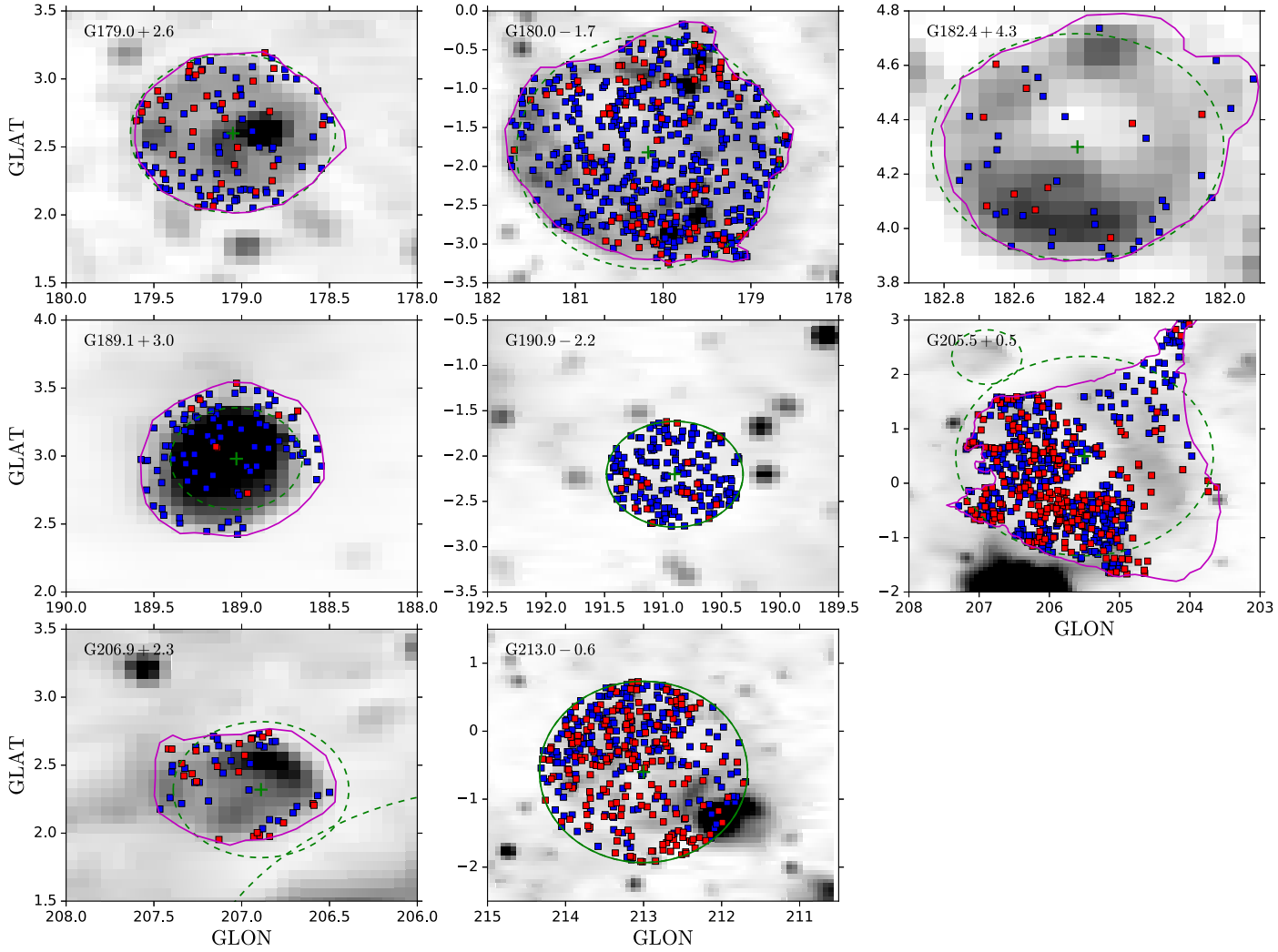

Figure 5. (Continued.)

platform afterwards toward G178.2–4.2 (Level C) supports our estimate of distance < 0.3 kpc. Moreover, our upper limits of distances for SNRs in Level B are consistent with this dust map as well. For G116.5+1.1, the position (∼0.7 kpc) of the extinction jump is highly consistent with our nearest tracer (0.68 kpc), so we also suggest 0.68 kpc as a possible distance of this SNR, noted in Table 4.

Because the LAMOST and APOGEE spectroscopic surveys are limited by stellar brightness, our star sample cannot provide the reddening profile with high spatial resolution. Therefore, for most of the cases, we can only derive the extinction jump for the whole SNR, rather than inferring a two-dimensional extinction map. If the dust in the SNR leads to a significant extinction jump along the sightline, accurate measurements can be made. For the SNRs with low extinction and within a complex interstellar environment, like G180.0–1.7, we cannot select specific fields like Chen et al. (2017) to reveal the SNR behind a huge foreground MC. 3D extinction maps help us revise our results. On the other hand, the stellar parameters from spectroscopy determine more accurately stellar reddening than the photometric colors. In the future, an expansion of the sample and an improvement of the method can be expected in combination with 3D dust maps.

4.1.2. Comparison with Distances Measured by Other Methods

Besides the 3D extinction analysis, some other methods are applied to estimate the distances to SNRs. First, the kinematic method based on the H I and/or CO absorption lines and the rotation curve of the Milky Way is widely used. This method suffers the ambiguity problem in the inner disk and large uncertainty in the outer disk. Second, the distance to the SNR can be inferred from the associated objects with known distances, such as OB stars (Humphreys 1978), MCs (Gerardy & Fesen 2007), or pulsars (Kramer et al. 2003). The uncertainty of this method comes from both the identification of the association and the distance of the associated objects. Third, extinction measurements based on red clump (RC) stars can trace the distances (e.g., Durant & van Kerkwijk 2006; Shan et al. 2018). Fourth, the empirical relation between surface brightness (Σ) and physical diameter (D) of the SNRs ($\Sigma - D$ relation) is often adopted to obtain SNR distance as well. The dispersion of the relation brings about uncertainty and the faintness of the object would bear more uncertainty. Fifth, the Sedov estimate can be made for some shell-type SNRs with X-ray observations for which the inhomogeneity of the ISM complicates the result. Others include the calculation of distance using proper motion (Boumis et al. 2004) or shock

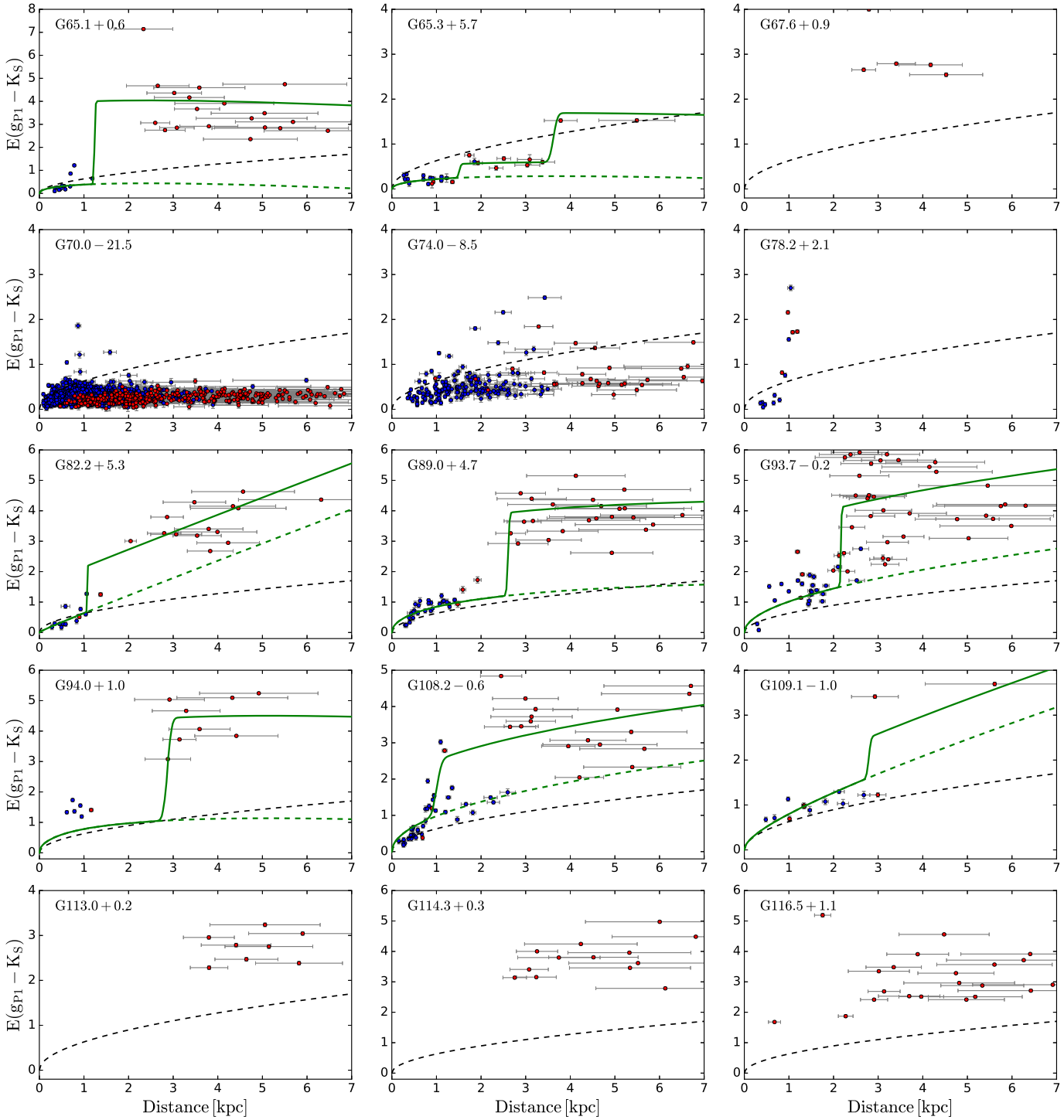

Figure 6. Color excess values $E(g_{P1} - K_S)$ vs. distances (in kpc) in the selected regions for all 32 SNRs. The blue and red dots represent dwarf and giant stars, respectively. The black dashed line is the derived common ISM reddening profile from the *l*165 region. The green solid lines are the best-fitting reddening profiles based on the sample stars. The green dashed lines decodes the ISM contribution derived from the extinction-distance model.

velocity (Blair et al. 2005). The error analysis will be addressed in greater detail for individual objects in the Appendix.

We found about 53 measurements in the literature for 22 SNRs in Level A (15) and B (7) with seven methods (the six methods mentioned above plus that of Yu et al. 2019). The comparison between our estimates and the distances in the literature is shown in Tables 2 and 3 and Figure 8 where different methods are in different colors and illustrated in the legends ("Others" indicates three works based on proper motion or shock velocity). The comparison with Yu et al. (2019) has been discussed in Section 4.1.1. Figure 8 visually exhibits the large dispersion between literature measurements as well as the large uncertainty in many cases. Thus, there is no possibility for our measurements to coincide with all previous results. On the contrary, discrepancy is expected.

The kinematic method is the most widely used, which accounts for over a third of the gross (18/53). Good agreements can be found for some cases like G109.1−1.0,

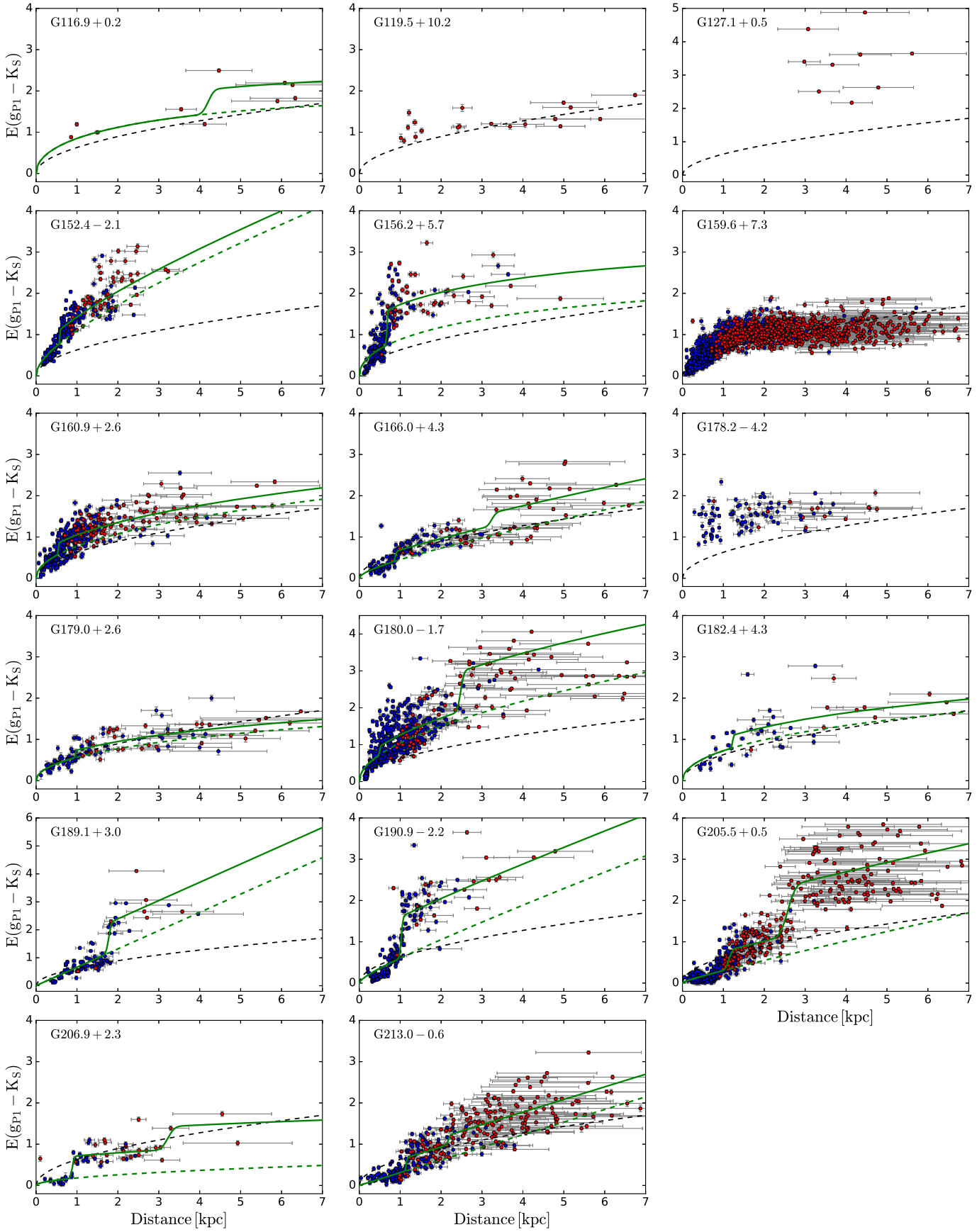

Figure 6. (Continued.)

Table 2
Distances of SNRs in Level A

SNR Names	$D_{\rm thiswork}$ (kpc)	$D_{\rm literature}$ (kpc)	Method	References
G78.2+2.1	0.98	1.7–2.6, 1.5 ± 0.4	associated object	1, 2
G89.0+4.7	2.3 ± 0.3	$1.9^{+0.3}_{-0.2}$, 0.80 ± 0.07, 1.0–1.6	RCs[a], associated object, $\Sigma - D$	3–8
G93.7–0.2	2.16 ± 0.02	1.5 ± 0.2	kinematics	9
G94.0+1.0	2.53 ± 1.08	4.5	associated object	10
G109.1–1.0	2.79 ± 0.04	3.0, 4.0 ± 0.8, 6.0	kinematics, RCs	11–13
G152.4–2.1	0.59 ± 0.09	1.1 ± 0.1, $\leqslant$**1.0**	kinematics, extinction	14, **32**
G156.2+5.7	0.68 ± 0.20	0.3, 1–3, 1.3, 3	associated object, kinematics, Sedov estimate	15–18
G160.9+2.6	0.54 ± 0.10	0.8 ± 0.4, 1.1, 1.3–1.8, $\geqslant$1.1, **0.6**	kinematics, Sedov estimate, $\Sigma - D$, associated object, extinction	19, 20, 7, 21, **32**
G166.0+4.3	3.24 ± 0.03	4.5 ± 1.5	kinematics	22
G182.4+4.3	1.05 ± 0.24	$\geqslant$3, ∼**1.1**	Sedov estimate, extinction	23, **32**
G189.1+3.0	1.80 ± 0.05	0.7–1.5, 1.9, 1.5, $\mathbf{1.73}^{+0.13}_{-0.09}$	kinematics, $\Sigma - D$, associated object, extinction	21, 24, 7, 8, 25, **32**
G190.9–2.2	1.03 ± 0.01	1.0 ± 0.3, $\mathbf{1.03}^{+0.02}_{-0.08}$	kinematics, extinction	26, **32**
G205.5+0.5	1.13 ± 0.01	1.6 ± 0.3, 1.6, 1.5, $\mathbf{0.93}^{+0.05}_{-0.08}/\mathbf{1.26}^{+0.09}_{-0.10}$	$\Sigma - D$, extinction	27–29, **32**
G206.9+2.3	0.89 ± 0.02	3–5, 1.6	$\Sigma - D$, kinematics	28, 30
G213.0–0.6	1.09 ± 0.29	∼1.0, 2.4, **1.15** ± 0.08	kinematics, associated object, extinction	30, 31, **32**

Note.
[a] Red clump stars.

References. (1) Leahy et al. (2013), (2) Landecker et al. (1980), (3) Shan et al. (2018), (4) Humphreys (1978), (5) Willis (1973), (6) Clark & Caswell (1976), (7) Caswell & Lerche (1979), (8) Milne (1979), (9) Uyaniker et al. (2002), (10) Foster (2005), (11) Kothes et al. (2002), (12) Tian et al. (2010), (13) Durant & van Kerkwijk (2006), (14) Foster & Cooper (2010), (15) Gerardy & Fesen (2007), (16) Reich et al. (1992), (17) Yamauchi et al. (1999), (18) Pfeffermann et al. (1991), (19) Leahy & Tian (2007), (20) Leahy (1987), (21) Lozinskaya (1981), (22) Landecker et al. (1989), (23) Kothes et al. (1998), (24) Ambrocio-Cruz et al. (2017), (25) Fesen (1984), (26) Foster et al. (2013), (27) Davies et al. (1978), (28) Graham et al. (1982), (29) Leahy et al. (1986), (30) Su et al. (2017), (31) Stupar & Parker (2012), (32) Yu et al. (2019).

Table 3
Distances of SNRs in Level B

SNR Names	$D_{\rm thiswork}$ (kpc)	$D_{\rm literature}$ (kpc)	Method	References
G65.3+5.7	1.51 ± 0.04	0.77 ± 0.20	proper motion	1
G74.0–8.5	<1.0	0.77, $0.54^{+0.01}_{-0.008}$, 0.735 ± 0.025	kinematic, shock velocity, associated object	2–4
G82.2+5.3	1.34 ± 0.13	1.6–3.3, 1.6, 3.2 ± 0.4	Sedov estimate, expansion velocity, RCs	5–7
G108.2–0.6	1.02 ± 0.01	3.2 ± 0.6	kinematics	8
G113.0+0.2	<3.8	3.1	kinematics	9
G116.9+0.2	4.3 ± 0.2	1.6, 4.2	kinematics	10, 11
G127.1+0.5	<2.9	0.3/1.3, 1.15	associated object, kinematics	12, 13

References. (1) Boumis et al. (2004), (2) Minkowski (1958), (3) Blair et al. (2005), (4) Fesen et al. (2018), (5) Mavromatakis et al. (2004), (6) Rosado & Gonzalez (1981), (7) Shan et al. (2018), (8) Tian et al. (2007), (9) Kothes et al. (2005), (10) Yar-Uyaniker et al. (2004), (11) Fich (1986), (12) Zhou et al. (2014), (13) Leahy & Tian (2006).

G189.1+3.0, and G190.9−2.2, while large discrepancies exist as well. In the direction of Galactic anticenter, the kinematic method tends to gain larger distances, which may be caused by the deviation due to noncircular motion (Tian & Leahy 2012) or the larger uncertainty of the rotation curve in the outer disk in comparison with inner disk due to invalidity of the tangent velocity method. The kinematic method suffers the well-known ambiguity problem as well. Ten estimates derived from the associated objects show the difference with our results on a similar level to the kinematic method. Distance measurements based on RC stars are mainly applicable to the SNRs in the first and fourth quadrants of the Milky Way because RC stars are much less abundant toward Galactic anticenter. So only 3 of 22 SNRs are studied with the RC stars. Two of them (G82.2+5.3 and G109.1–1.0) yielded much larger distances than ours as well as other results, and the estimate to G89.0+4.7 is comparable to ours. Distances derived from the $\Sigma - D$ relation (seven cases) are much closer to our estimates compared to the results with methods of kinematics and associated objects. The five Sedov estimates all yield distances larger than ours. The three studies based on proper motion or shock velocity provide some informative restrictions on the SNRs in Level B whose distances are not well determined in this study. The detailed analysis of the differences can be found in the Appendix.

4.1.3. Distribution in the Galactic Plane

With the measured distances, Figure 9 shows the spatial distribution of 22 SNRs in Level A and B projected on the Galactic plane. Due to the limits of the APOGEE and LAMOST spectroscopic surveys, most of the SNRs under

Table 4
Distances of SNRs in Level C

SNR Names	$D_{\rm thiswork}$ (kpc)	$D_{\rm literature}$ (kpc)	Method	References
G65.1+0.6	1.33 ± 0.60	9.2	kinematics	1
G67.6+0.9	<2.6	3.2 ± 0.4	RCs	2
G70.0–21.5	···	1–2	shock velocity	3
G114.3+0.3	<2.7	0.7, 3.4, 4.2	kinematics	4–6
G116.5+1.1	<3.0/0.68	1.6, 3.6–5.2, 4.2	kinematics	4–6
G119.5+10.2	···	1.4 ± 0.3	kinematics	7
G159.6+7.3	···			
G178.2–4.2	<0.3/>5.0			
G179.0+2.6	0.92 ± 0.04	3.5, 6.1, 2.9, 3.1	$\Sigma - D$	8–11
G180.0–1.7	0.38 ± 0.10	1.06, 0.9, 0.8–1.37, 1.6 ± 0.3, 1.2, $1.47^{+0.42}_{-0.27}$, $1.3^{+0.22}_{-0.16}$, $1.333^{+0.103}_{-0.112}$, 1.22 ± 0.21	$\Sigma - D$, pulsar distance, pre-companion, extinction	10, 12, 13, 14, 15–17, 18, 19

References. (1) Tian & Leahy (2006), (2) Shan et al. (2018), (3) Fesen et al. (2015), (4) Yar-Uyaniker et al. (2004), (5) Reich & Braunsfurth (1981), (6) Fich (1986), (7) Pineault et al. (1993), (8) Fuerst & Reich (1986), (9) Case & Bhattacharya (1998), (10) Guseinov et al. (2003), (11) Pavlovic et al. (2014), (12) Clark & Caswell (1976), (13) Kundu et al. (1980), (14) Sofue et al. (1980), (15) Kramer et al. (2003), (16) Ng et al. (2007), (17) Chatterjee et al. (2009), (18) Dinçel et al. (2015), (19) Chen et al. (2017).

investigation are in the second and third quadrants of the Milky Way. It can be seen that the SNRs are mainly located in the Local arm. Six SNRs are suggested to reside in the Perseus arm. Three cases, i.e., G89.0+4.7, G93.7−0.2, and G94.0+1.0, are found between the two arms.

4.2. The Extinction Curve

The extinction curves vary from one sightline to another, revealing the wavelength-dependent extinction law in different environments. As the absolute extinction is usually difficult to measure and uncertain, we use the color excess ratios (CERs), i.e., $E(g_{\rm P1} - \lambda)/E(g_{\rm P1} - r_{\rm P1})$, to represent the extinction curves for the sightlines to the 32 SNRs, as well as the "*l*165" and the Rosette Nebula. For SNRs whose reddening profiles were well model-fitted, the color excess is then δA in Equation (3)—the amplitude of the extinction jump at a given color. For the other SNRs, we first calculate the color excesses for individual sample stars in and behind the SNRs by subtracting the foreground ISM contribution according to the reddening profiles of "*l*165," and then derive the CERs by proportional fitting to the color excesses $E(g_{\rm P1} - \lambda)$ and $E(g_{\rm P1} - r_{\rm P1})$. Because the stars toward G70.0–21.5 and G159.6+7.3 show lower extinctions than the sightline of "*l*165," no subtraction is performed for these two sightlines, which can bring about uncertainties in the subsequent results.

To characterize the properties of SNR dust, the CCM89 formula (Cardelli et al. 1989) and a simple dust model are applied to fit the extinction curves. In total, from $G_{\rm BP}$ to $WISE/W_2$, we have 10 CERs for the fittings. But Wang & Chen (2019) reported significant amount of curvature of CERs (the deviation from the linear relationship between two color excesses for highly reddened stars) for the *Gaia* bands for heavily reddened stars because of their broad bandwidths. Since the correction for the curvature needs stellar intrinsic flux distribution that is unavailable, G and $G_{\rm BP}$ are removed in further fitting, while $G_{\rm RP}$ is usable due to its longer wavelength and is much less affected. Because the APASS and Pan-STARRS1 filters cover the wavelength range of *Gaia*, the removal of the two *Gaia* bands should not change the result. Therefore, the fitting is performed to the other eight CERs.

4.2.1. CCM89

Cardelli et al. (1989) presented a one-parameter model (CCM89) to approximate the various extinction curves, which received wide application. CCM89 is characterized by the ratio of the total extinction to the selective extinction $R_{\rm V} = A_{\rm V}/E(B - V) = A_{\rm V}/(A_{\rm B} - A_{\rm V})$. With the derived CERs, $R_{\rm V}$ is sampled from 1 to 10 with a step of 0.01 to find the best-fit for each SNR. A Monte Carlo simulation based on the values and errors of the CERs determines the uncertainty of $R_{\rm V}$. The best-fit $R_{\rm V}$ values are shown in Table 5 together with the error.

For 18 cases, $R_{\rm V}$ value ranges between 3.1 and 5.5, while for 10 other sightlines $R_{\rm V} < 3.1$. There are four SNRs with $R_{\rm V} > 5.5$: $R_{\rm V} = 5.98$ for G213.6–0.6, $R_{\rm V} = 6.44$ for G108.2–0.6, $R_{\rm V} = 6.61$ for G166.0+4.3, and the largest $R_{\rm V}$ of 7.71 for G179.0+2.6. But for G179.0+2.6, its CERs show a dramatic rise in the $i_{\rm P1}$ and $G_{\rm RP}$ bands, following a platform in IR bands; indeed, the CCM89 formula cannot reasonably characterize this queer curve, and the resultant $R_{\rm V}$ of 7.71 is unreliable.

4.2.2. The Simple Dust Model

CCM89 is a mathematical formula, which cannot tell the dust properties and, as shown above, fails in some cases. Besides, CCM89 is derived mainly from the extinction curves in the UV and optical bands, and significant deviations appear in the IR bands, which occurs in our fitting. Such deviation can also be seen from comparing the CCM89 law and the WD01 (Weingartner & Draine 2001) model in Figure 10 at $R_{\rm V} = 3.1$, 4.0 and 5.5, respectively. The comparison shows that CCM89 yields a smaller $R_{\rm V}$ value for a given extinction curve, and the differences increase with $R_{\rm V}$. In order to better fit the derived extinction as a function of waveband, we build a simple dust model.

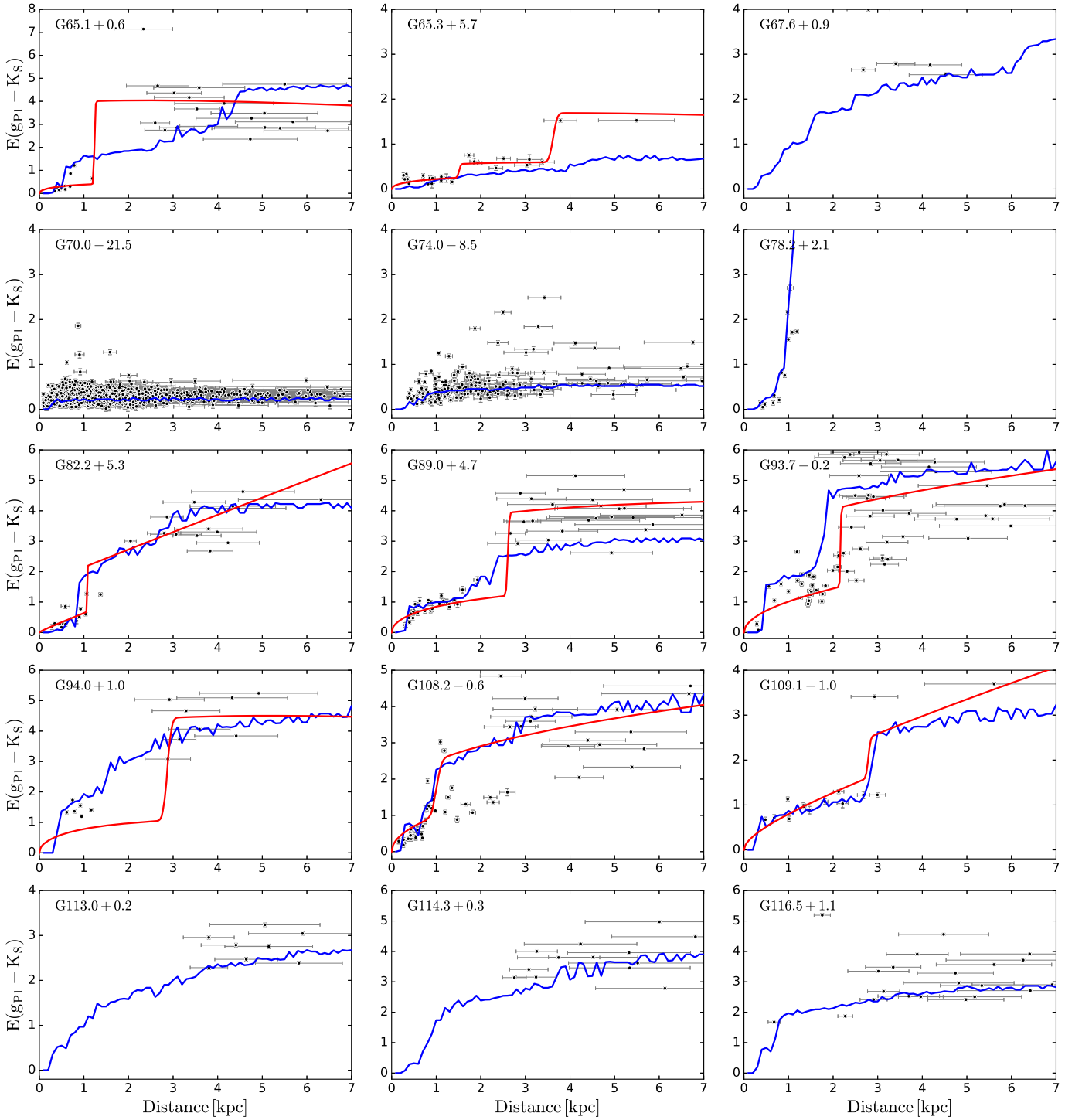

Figure 7. The comparison between our results (black dots and red lines) and the reddening profiles (blue lines) retrieved from the dust map by Green et al. (2019). The black dots and red lines are the same as the blue/red dots and green lines in Figure 6, respectively.

Because the derived extinction curves do not have enough observational points or wavelength coverage to constrain the relatively numerous parameters of WD01, a simpler dust model is applied to the extinction curves. This model considers two main species of the dust in ISM: graphite and silicate. To simplify the model, their mass ratio is fixed as $M_{\rm sil}/M_{\rm gra} = 2{:}1$. The size distributions of both graphite and silicate grains follow the MRN model (Mathis et al. 1977), i.e., $n(a) \propto a^{-\alpha}$. The model is fixed by a power-law index of the grain size distribution $\alpha_{\rm gra}$ and $\alpha_{\rm sil}$ for graphite and silicate grains, respectively. For convenience of comparison, we defined the average size of dust grains by

$$\langle a \rangle = \frac{\int_{a_{\rm min}}^{a_{\rm max}} a \cdot n(a) da}{\int_{a_{\rm min}}^{a_{\rm max}} n(a) da}, \quad (5)$$

where $a_{\rm min}$ and $a_{\rm max}$ are 0.005 μm and 0.25 μm, respectively. The fitting results are shown in Table 5 and Figure 11. As only the indexes for the dust size distribution power law are

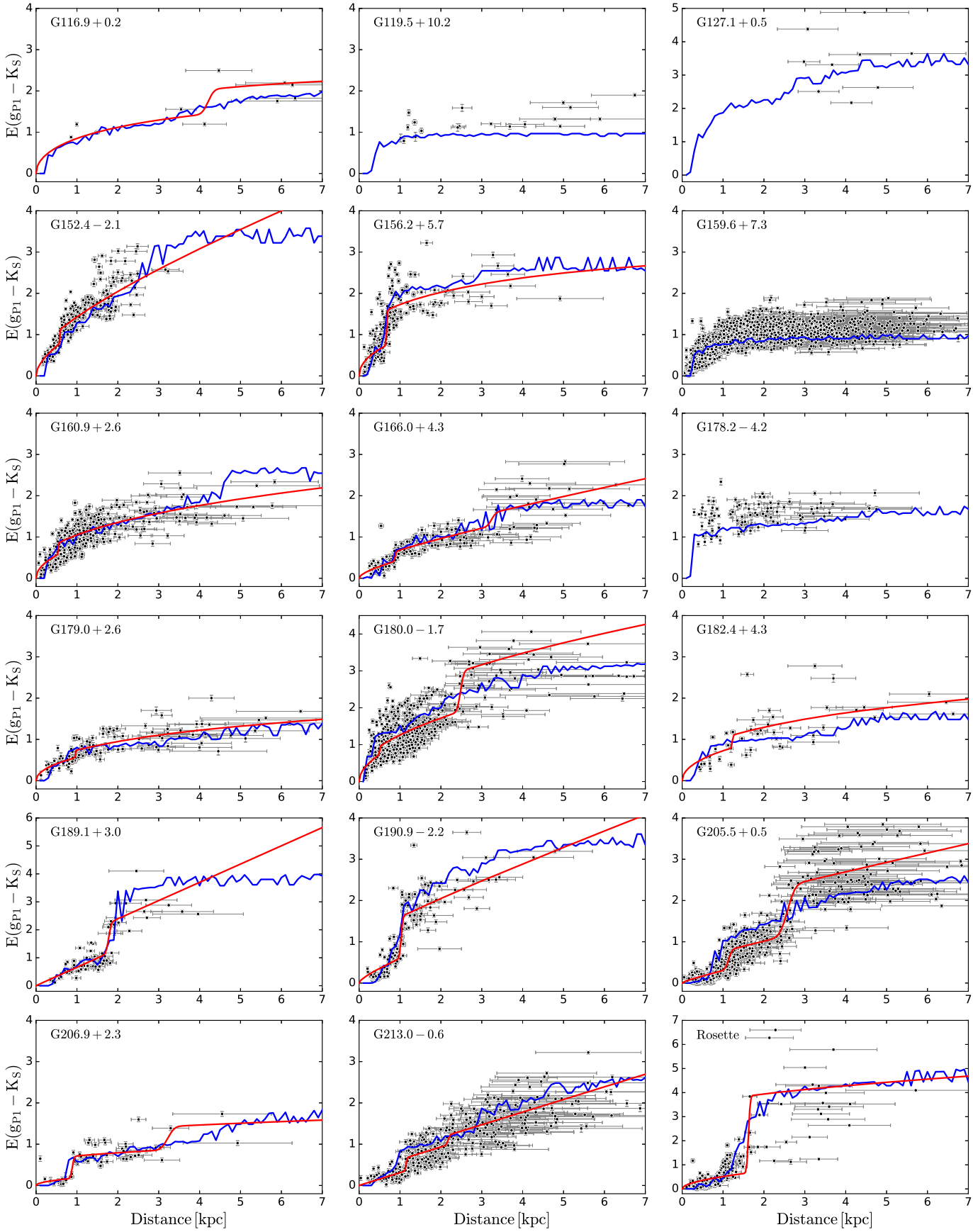

Figure 7. (Continued.)

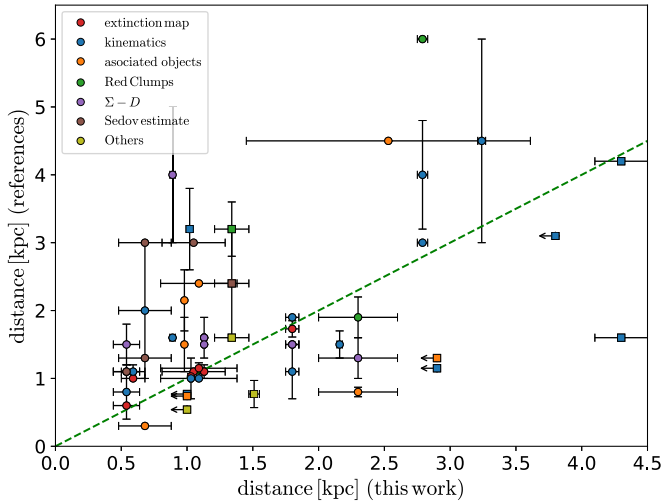

Figure 8. The comparison between our results and the distances measured by other methods for SNRs in Level A and B. Dots and squares decode SNRs in Level A and B, respectively. Squares with left arrows are the cases with distance upper limits. Colors stand for different methods illustrated in the legends. "Others" means the methods based on proper motion or shock velocity. Dots without error bars along the *y*-axis means no error analysis in the corresponding literature. The green dashed line traces the one-to-one correspondence.

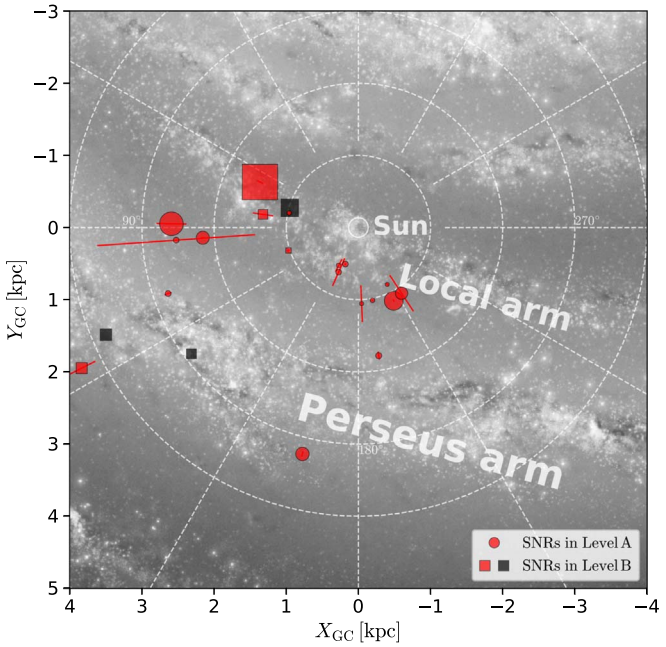

Figure 9. A face-on view of the distribution of the SNRs in Level A (15) and B (7). The red dots and squares with error bars show the measured distances and uncertainties. The black squares are the cases with distance upper limits. The sizes are proportional to their diameters. The background image, created by Robert Hurt in consultation with Robert Benjamin (Churchwell et al. 2009), is centered at the Sun, with the Galactic Center in the upward direction.

adjustable, the fitting fails for seven SNRs. All of the other 25 SNRs yield larger R_V values than that by CCM89, and generally, their differences increase with R_V (see Figure 12), which resembles the situation of the difference between the CCM89 formula and the WD01 model.

The following discussions are based only on the 22 SNRs in Level A/B with reliable distance measurements while those in Level C are not included. The fitted R_V value is >3.23 (the value for the diffuse "*l*165" region) for 13 SNRs, and >4.50 for six SNRs. Generally, the value of R_V increases with the grain size because the larger grains is more efficient in extinction at longer wavelength. Figure 13 displays the R_V values from our dust model as a function of the average radii of the graphite ($\langle a\rangle_{gra}$) and silicate ($\langle a\rangle_{sil}$) grains, respectively. All of the SNRs except G108.2–0.6 have the average radius of graphite grains $\langle a\rangle_{gra} \sim 0.008\,\mu$m. In contrast, $\langle a\rangle_{sil}$ varies from 0.007 to 0.16 μm, mostly much larger than $\langle a\rangle_{gra}$. In comparison, the Rosette Nebula and the "*l*165" region have $\langle a\rangle_{sil}$ very close to their $\langle a\rangle_{gra}$, both are either 0.008 μm or 0.009 μm. If the dust toward the "*l*165" region with $R_V = 3.23$ is typical for diffuse ISM, it may be concluded that the average size of the silicate grains in SNRs is bigger than that in diffuse ISM; although, the graphite grains are comparable to those in diffuse ISM. This large size of silicate grains leads to the larger R_V values since silicate grains constitute two-thirds of the dust in the model and, thus, are dominant contributors to the extinction. The model of Nozawa et al. (2007) suggested that silicate dust is more easily destroyed by SN explosion than carbonaceous dust. The apparent increase of $\langle a\rangle_{sil}$ in some SNRs may be explained by the destruction of small silicate grains by the sputtering process. Together with the detection of SiO line emission in shocks (Guillet et al. 2009), the large size of silicate grains supports the idea that the very small silicate grains may be destroyed during the SN explosion. It is true that much larger $\langle a\rangle_{sil}$ than $\langle a\rangle_{gra}$ is obtained for the Level A SNRs. On the other hand, the ratio of the graphite to silicate grain size could diagnose whether the detected extinction jump is caused by the SNR such as in the cases of G93.7–0.2, G156.2+5.7, and G206.9+2.3 (Section 4.1); although, the distance is still uncertain because of the limitation of our simple dust model and the influence of the ambient ISM in particular for the large SNRs. Meanwhile, some SNRs in Level B with apparent extinction jumps have a similar radius of $\langle a\rangle_{gra}$ and $\langle a\rangle_{sil}$ that is comparable to the diffuse ISM, e.g., G82.2+5.3, which may question the credibility that the extinction is caused by the SNR. G108.2–0.6 is a special case with the largest $\langle a\rangle_{gra}$ (0.025 μm) comparable to its $\langle a\rangle_{sil}$ (0.022 μm). It may be argued that what the R_V value reflects is the property of the dust in the MCs where the SNRs reside. This possibility is difficult to rule out. But since we are confined to the SNR region other than the whole MC, the dust, even from the MCs, should have been processed by the SN explosion. They may be called the SN processed dust in MCs. Moreover, the normal extinction curve of the MCs can usually be represented well by the CCM89 curve, while the extinction curves derived here usually deviates apparently from the CCM89 curve. These dust should have been influenced by the SN explosion to some extent.

If we assume a similar ambient ISM environment for all the SNRs, which is certainly very rough, the diameter is then positively correlated with the age of the SNR. In order to know if R_V depends on evolution of the SNR, the distribution of R_V with the SNR diameter (D) is shown in Figure 14, where D is calculated from the distance (d) and the major angular diameter (θ), $D = d \times \sin(\theta)$. It can be seen that the largest values of R_V occur only for small SNRs that have a diameter

Table 5
Fitting Results to the Extinction Curves of 32 SNRs, as well as "*l*165" and the Rosette Nebula

SNR	Level[a]	R_V [CCM89]	R_V [Dust Model]	α_{gra}	α_{sil}	$\langle a\rangle_{gra}$[b] (μm)	$\langle a\rangle_{sil}$[c] (μm)
G65.1+0.6	C	$3.75^{+0.08}_{-0.09}$	3.99	3.15	2.93	0.0093	0.0101
G65.3+5.7	B	4.55 ± 0.26	4.97	2.85	2.08	0.0105	0.0185
G67.6+0.9	C	$2.99^{+0.06}_{-0.07}$	3.27	3.95	2.16	0.0076	0.0170
G70.0–21.5	C	$2.30^{+0.03}_{-0.02}$	2.44	4.43	3.30	0.0071	0.0088
G74.0–8.5	B	2.79 ± 0.23	…	…	…	…	…
G78.2+2.1	A	$4.03^{+0.40}_{-0.38}$	4.47	3.29	1.69	0.0088	0.0283
G82.2+5.3	B	3.41 ± 0.25	3.61	3.35	3.18	0.0087	0.0091
G89.0+4.7	A	$4.29^{+0.16}_{-0.15}$	4.86	3.87	−0.82	0.0077	0.1615
G93.7–0.2	**A**	3.99 ± 0.07	4.50	3.65	0.64	0.0080	0.0869
G94.0+1.0	A	$3.81^{+0.44}_{-0.42}$	4.22	3.36	1.90	0.0086	0.0223
G108.2–0.6	B	$6.44^{+0.41}_{-0.40}$	6.74	1.78	1.90	0.0253	0.0222
G109.1–1.0	A	$3.44^{+0.42}_{-0.38}$	…	…	…	…	…
G113.0+0.2	B	3.40 ± 0.15	3.78	3.83	1.45	0.0077	0.0376
G114.3+0.3	C	$3.48^{+0.07}_{-0.06}$	3.82	3.50	2.19	0.0083	0.0166
G116.5+1.1	C	3.36 ± 0.08	3.73	3.80	1.62	0.0078	0.0308
G116.9+0.2	B	$3.02^{+0.27}_{-0.25}$	…	…	…	…	…
G119.5+10.2	C	$2.71^{+0.44}_{-0.43}$	…	…	…	…	…
G127.1+0.5	B	$3.36^{+0.11}_{-0.10}$	3.73	3.82	1.56	0.0077	0.0329
G152.4–2.1	A	2.52 ± 0.23	2.62	4.05	3.81	0.0074	0.0078
G156.2+5.7	A	$5.08^{+0.31}_{-0.32}$	5.79	3.21	0.13	0.0091	0.1204
G159.6+7.3	C	2.81 ± 0.01	2.97	3.78	3.37	0.0078	0.0086
G160.9+2.6	A	2.86 ± 0.15	2.92	3.88	4.36	0.0077	0.0071
G166.0+4.3	A	$6.61^{+0.54}_{-0.51}$	…	…	…	…	…
G178.2–4.2	C	$3.11^{+0.07}_{-0.08}$	3.33	3.59	2.95	0.0081	0.0100
G179.0+2.6	C	$7.71^{+0.72}_{-0.67}$	…	…	…	…	…
G180.0–1.7	C	3.28 ± 0.29	3.33	3.84	5.39	0.0077	0.0065
G182.4+4.3	A	$4.78^{+0.35}_{-0.34}$	5.33	2.94	1.44	0.0101	0.0378
G189.1+3.0	A	$3.67^{+0.17}_{-0.16}$	4.05	3.42	2.01	0.0085	0.0198
G190.9–2.2	A	2.79 ± 0.06	3.00	3.91	2.82	0.0076	0.0107
G205.5+0.5	A	4.01 ± 0.16	4.50	3.52	1.01	0.0083	0.0618
G206.9+2.3	A	$2.81^{+0.20}_{-0.19}$	3.02	3.86	2.92	0.0077	0.0102
G213.0–0.6	A	$5.98^{+0.46}_{-0.45}$	…	…	…	…	…
Rosette	…	3.46 ± 0.04	3.57	3.38	3.76	0.0086	0.0078
"*l*165"	…	$3.05^{+0.02}_{-0.03}$	3.23	3.59	3.34	0.0081	0.0087

Notes.
[a] The quality of the distance measurement.
[b] The average size of the graphite grains.
[c] The average size of the silicate grains.

less than or around 20 pc. According to Draine (2011), the radius of an SNR under typical interstellar conditions ranges from ∼5 to 24 pc during the Sedov–Taylor phase; thus, these relatively smaller SNRs are in the early Sedov–Taylor phase. In principle, large R_V implies large grains, which may be explained by destruction of small particles by the shock wave. On the other hand, there are quite a few SNRs with small R_V, which cannot be explained by this mechanism. The larger SNRs with $D > 40$ pc lack very large R_V values but mostly around 4.5, systematically higher than the mean value for diffuse ISM. These large SNRs should be relatively old and thin; thus, the results may suffer more uncertainty than the small SNRs. With age, the SNR expands and sweeps up more ambient interstellar dust, which would erase away the features of the SN ejecta. In addition, the shock wave slows down with age, and its influence on the ambient dust weakens. Consequently, the dust in the SNRs would look more like the ambient interstellar dust. However, as we discussed in Section 1, the effect of SN explosion on the grain size is complex, depending on the type of the SN explosion, the

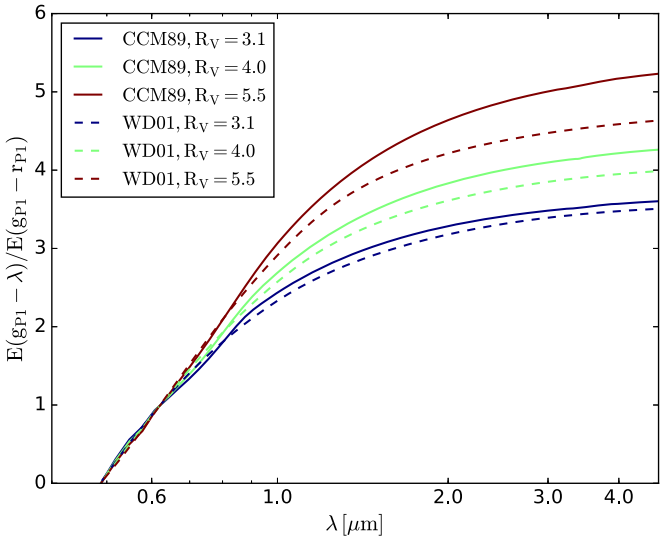

Figure 10. Comparison between the extinction curves calculated by CCM89 and WD01, with $R_V = 3.1$, 4.0, and 5.5.

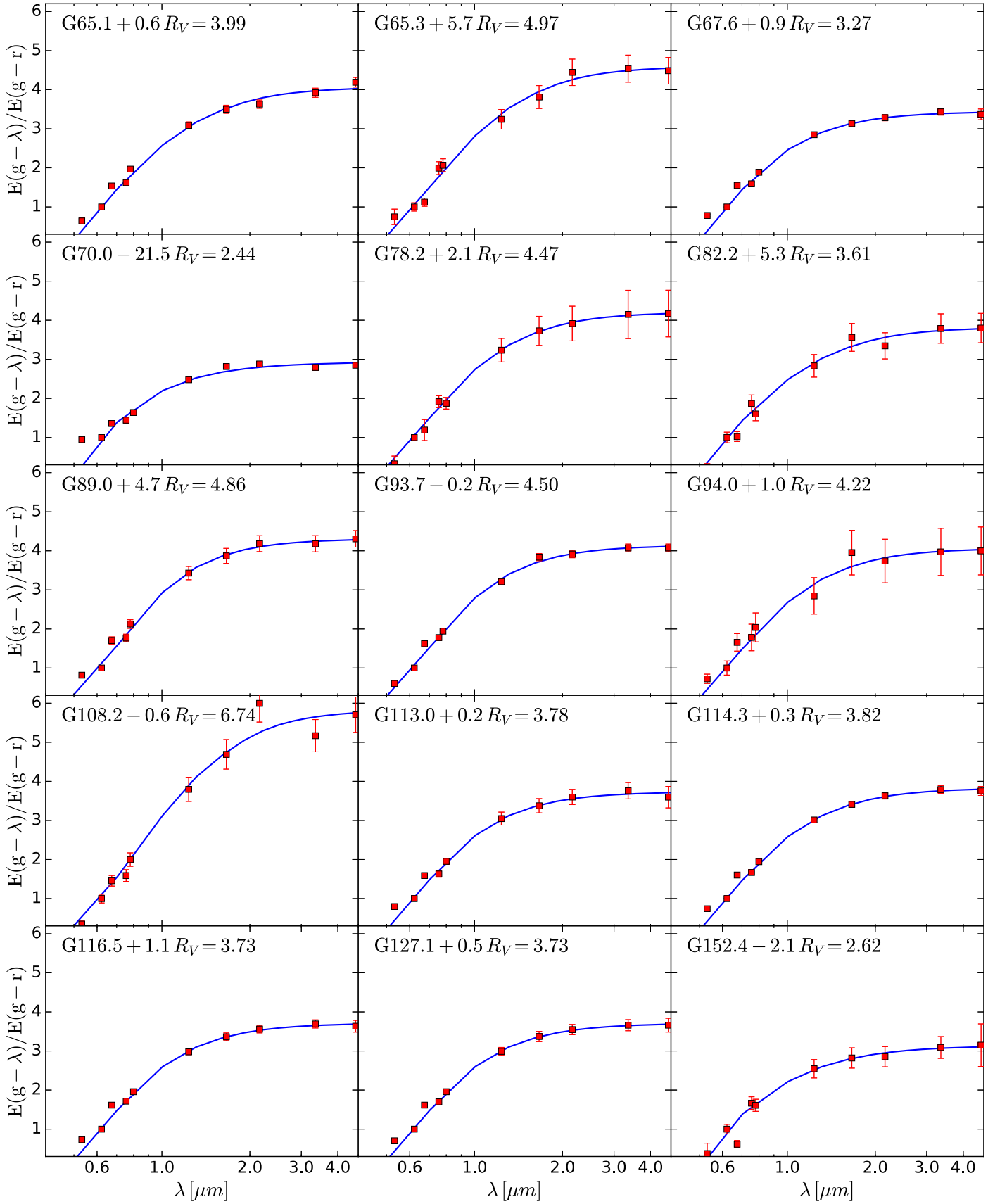

Figure 11. The extinction curves for 25 SNRs, as well as "*l*165" and Rosette Nebula. The red squares with error bars are the CERs calculated for 10 bands, which from right to left are G_{BP}, r_{P1}, G, i_{P1}, G_{RP}, J, H, K_S, W_1, and W_2, respectively. The blue lines are the best-fit results of our dust model.

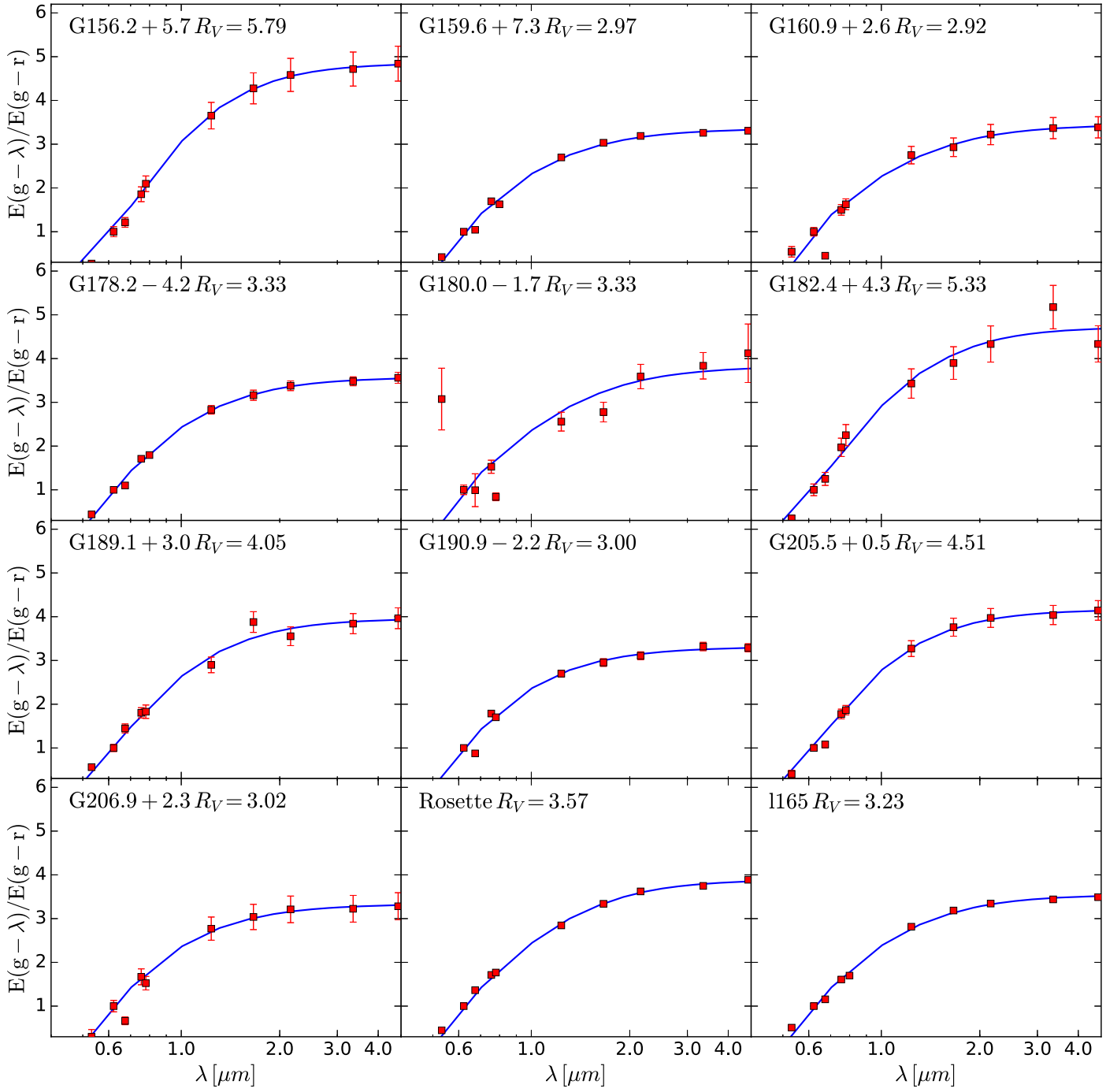

Figure 11. (Continued.)

environment, the dust species and grain size, etc. We will study in further detail the grain size distributions and the causes in a forthcoming paper.

4.3. Average Extinction Law of the Milky Way

The large star sample used in this work contains over 1.3 million sources. They have a wide spatial distribution, with decl. from -10° to 60° and distance beyond 15 kpc (mainly within 6 kpc). These stars cover various environments, including both very diffuse ISM and dense dust clouds with extinction as high as $E(g_{\rm P1} - K_{\rm S}) \approx 14.0$ mag. Therefore, the extinction law derived from this sample shall be very representative for the average ISM environment.

First, the color excesses for all of the stars at all 10 bands, i.e., $E(g_{\rm P1} - \lambda)$, are computed. Considering the photometric errors and the uncertainty of intrinsic colors, sources with color excesses smaller than -0.1 are dropped, and then a linear fitting is applied to derived CERs with $E(g_{\rm P1} - r_{\rm P1})$ as the reference color excess. Apparent curvatures appear in the color excess–color excess diagrams (Figure 15) for heavily reddened stars in the *Gaia* bands, which are discussed in detail by Wang & Chen (2019). Thus, the three *Gaia* bands are not used in deriving the average extinction law. Since the Pan-STARRS1 filters have

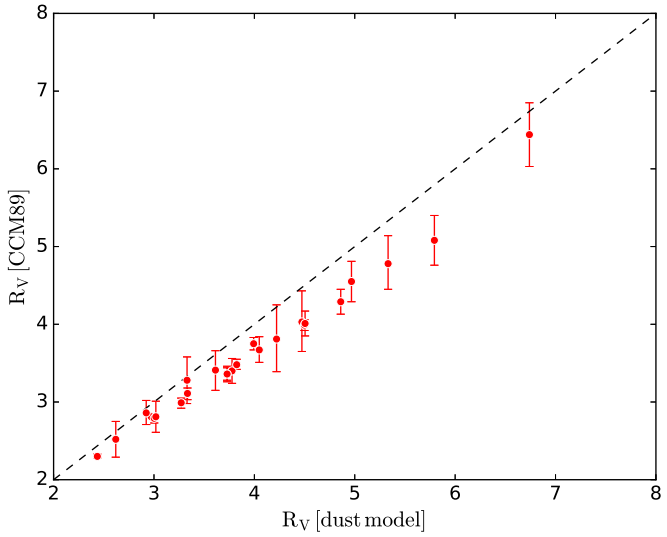

Figure 12. The comparison between R_V values fitted by the CCM89 formula and the dust model. The black dashed line traces the one-to-one correspondance.

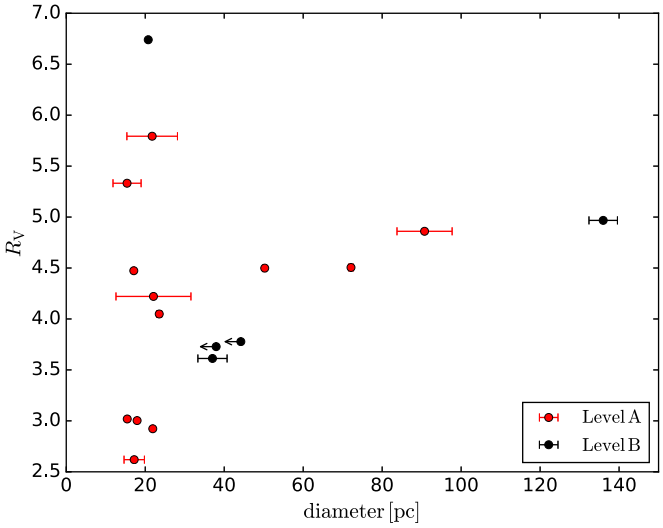

Figure 14. R_V values fitted by dust model as a function of the diameters of 22 SNRs in Level A (red dots) and B (black dots). The black dots with left arrows are the ones with upper distance limits.

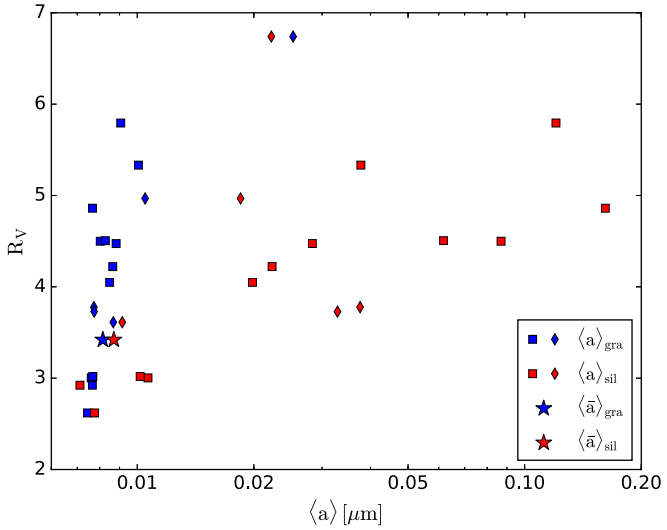

Figure 13. R_V values fitted by the dust model as a function of the average radii of graphite (in blue) and silicate (in red) grains, respectively, for 22 SNRs in Level A (squares) and B (diamonds). The big stars indicate the average of our Galaxy (see Section 4.3).

covered the *Gaia* waveband range, the results should not be influenced. The CCM89 law fitting to the CERs results in $R_V = 3.15$, very close to the average values suggested by other works (Draine 2003; Schlafly & Finkbeiner 2011). While our simple dust model yields a larger $R_V = 3.42$ as demonstrated earlier. In addition, the average radii of graphite and silicate grains are $\langle a \rangle_{gra} = 0.0082\ \mu$m, $\langle a \rangle_{sil} = 0.0087\ \mu$m, respectively, the same as the sizes toward the "*l*165" sightline (see Table 5), which confirms that the "*l*165" sightline is a typical diffuse ISM (Wang et al. 2017).

Wang & Chen (2019) suggested a modified CCM89 formula to trace the average extinction law. To fit the extinctions derived by using RC stars as standard candle, they re-determined the coefficients of the CCM89 formula. In their equations, the coefficients of high-order terms are neglected, which yielded a smoother curve than CCM89. In Figure 16, the average CERs (red squares) together with the dust model result (red line) derived here are compared with the traditional CCM89 law (black line) and the newly modified law by Wang & Chen (2019; blue line) with $R_V = 3.1$. In general, our law coincides with CCM89 from optical to NIR though becomes slightly flatter in the NIR. On the other hand, the IR extinction curve deviates from that of Wang & Chen (2019). This deviation is difficult to understand since both methods seem to calculate the color excesses accurately by subtracting the intrinsic color derived from spectroscopy. One possible reason is that we use various types of stars to trace the extinction, while Wang & Chen (2019) used only red clump stars; although, this should make no difference in deriving the extinction law.

5. Summary

This work conducted a systematic study of the distances to and the extinctions of Galactic SNRs from the change of extinction with distance of the stars toward the sightline of the SNR. Compared to Paper I, the methods are improved by two aspects. The first is that the metallicity effect is taken into account in addition to effective temperature and surface gravity when stellar intrinsic colors are determined. This improvement leads to more accurate intrinsic colors and correspondingly color excesses. The second is that stellar distance comes from the *Gaia* DR2 that shuns the uncertainties from the stellar model.

Incorporating the available data from the APOGEE and LAMOST spectroscopic surveys, the distance and the extinction from optical to NIR are studied for 32 Galactic SNRs. The distances to 14 SNRs in Level A are well determined by our extinction-distance model. The measured distance to G78.2 +2.1 is reliable because of its conspicuous extinction jump and classified as Level A object as well. In addition, the upper limits of distance to three SNRs are derived. In total, the distance estimation is provided for 22 SNRs mostly in the second and third quadrants. Our estimated distances are in

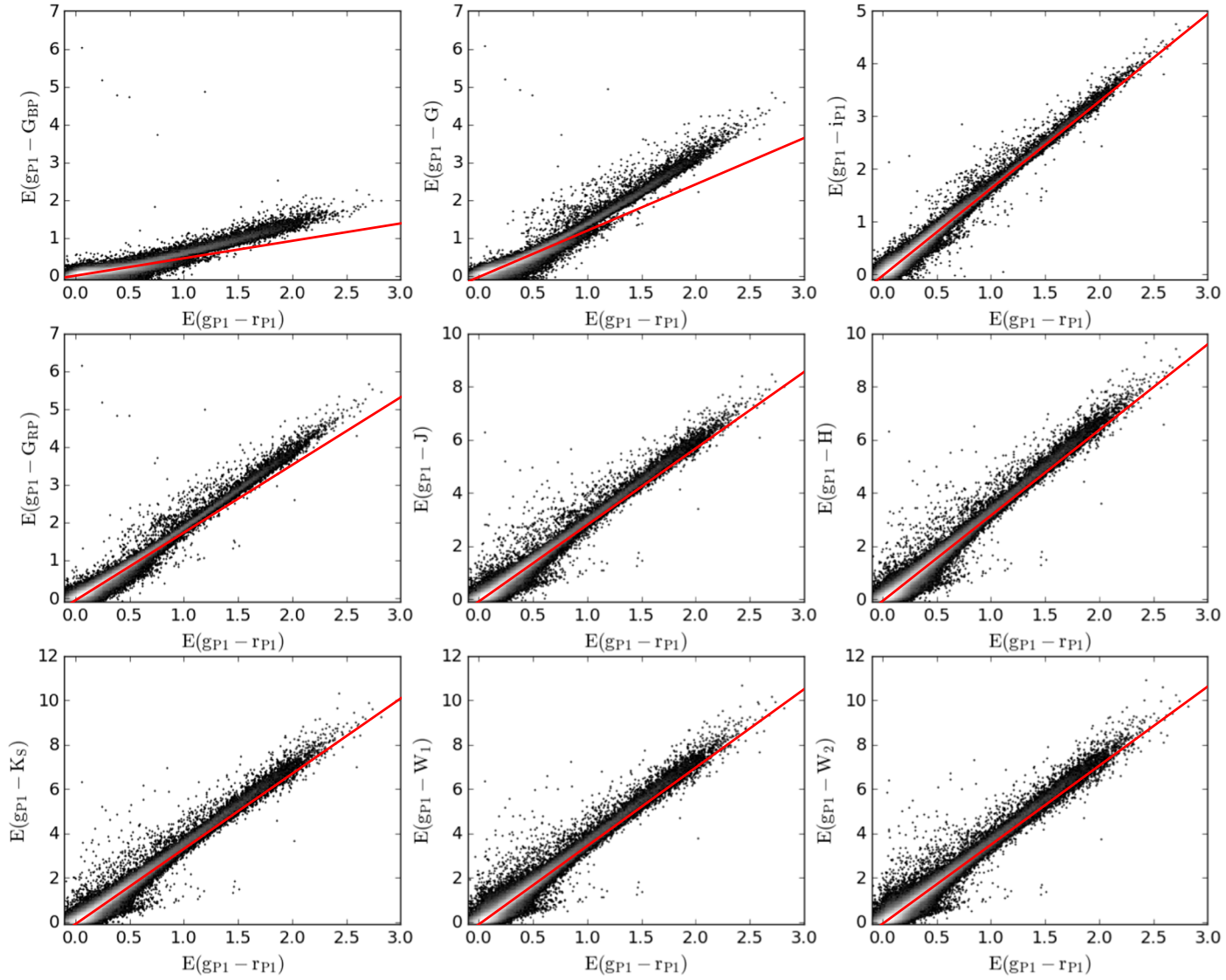

Figure 15. The color excess–color excess diagrams for our star sample. Red lines represent the best linear CERs fittings, and the grayscale map shows the number density of the sample stars.

general very consistent with the results derived from the 3D dust maps by Yu et al. (2019) and Green et al. (2019). Most of the investigated SNRs are located in the Local arm, with distances <2.0 kpc.

The extinctions of the SNRs expressed by the color excesses $E(g_{\rm P1}-\lambda)$ are either derived from the extinction-distance model or by taking the mean values of the extinctions of tracer stars. The wavebands used include the *Gaia*/$G_{\rm BP}$, G, and $G_{\rm RP}$, APASS/*gri*, and Pan-STARRS1/*gri*, 2MASS/$JHK_{\rm S}$, and *WISE*/W_1 and W_2 filters. The changes with waveband of the CERs $E(g_{\rm P1}-\lambda)/E(g_{\rm P1}-r_{\rm P1})$ are fitted by the CCM89 law and the deviation is apparent in some cases, in particular in the IR bands. A simple dust model is built to fit the observed CERs. It is found that the values of $R_{\rm V}$ range from about 2.4 to 6.7. The size of the SNR dust grains inferred from the model is bifurcated—while the graphite grains have an average radius around 0.008 μm comparable to the case in the diffuse ISM, the silicate grains are generally large with an average radius up to about 0.02–0.03 μm, which is significantly bigger than the grain size in the diffuse ISM. Although this phenomenon may be explained by the explanation that the silicate grains are more easily destroyed by the SN explosion, a careful study is needed to fully understand the reasons.

This work has two by-products. One is the relation of stellar intrinsic colors with effective temperature for both dwarf and giant stars in the bands from optical to NIR. The other is the average extinction law of our Galaxy from 1.3 million stars, which agrees with the CCM89 with $R_{\rm V}=3.15$ though slightly deviates in the NIR bands.

In the following work, we will investigate the dust properties by a more refined model, and the dust mass of the SNRs from the extinction and dust properties. Further, the influence of SN explosion on the interstellar dust will be discussed.

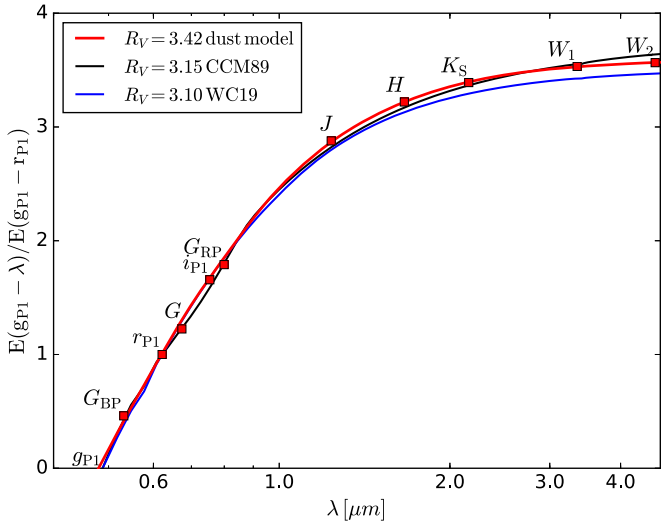

Figure 16. The average extinction curve of the Milky Way derived from our star sample. The red squares are calculated CERs at 10 bands, and the black line is fitted by CCM89. The blue line is a modified curve suggested by Wang & Chen (2019) with $R_V = 3.1$. The red line is fitted by our dust model. The *Gaia* bands, G_{BP}, G, and G_{RP}, are presented but are not considered during fitting.

We would like to thank Dr Jacco van Loon for his very careful reading of the paper and his comments and suggestions that helped to improve the paper effectively. We thank Drs Haibo Yuan and Mengfei Zhang for their useful suggestions. This work is supported by the National Natural Science Foundation of China through the project NSFC 11533002, and the China Scholarship Council (No.201806040200). This work has made use of data from the surveys by SDSS, LAMOST, *Gaia*, APASS, Pan-STARRS, 2MASS, and *WISE*.

Software: astropy (Astropy Collaboration et al. 2013), emcee (Foreman-Mackey et al. 2013).

Appendix
Discussion on the Distances to the Individual SNR

A.1. Level A

1. G78.2+2.1 is a nearby shell-type SNR, with two bright unresolved shells in the north and south (Gao et al. 2011a). From the H I absorption spectra, Leahy et al. (2013) determined the association of G78.2+2.1 and the H II region γ Cygni Nebula overlapping with the southern shell, and the distance to the SNR is then 1.7–2.6 kpc. An earlier study of another associated H II region IC 1318b suggested a distance of 1.5 ± 0.4 kpc (Landecker et al. 1980). There is no tracer farther than 1.2 kpc in our star sample so that the model fitting failed. Nevertheless, the tracers between 0.8 to 1.1 kpc display a very conspicuous extinction jump, which puts a strict constraint on its distance. We suggest the average distance of these tracers, 0.98 kpc, to be the distance to G78.2+2.1. Within the uncertainty range, this distance coincides with that of Landecker et al. (1980), who adopted the distance of the H II region IC 1318b.
2. G89.0+4.7 (HB21) was discovered by Hanbury Brown & Hazard (1953) at 159 MHz. HB21 has an irregular shell structure at radio wavelengths, with a well-defined outer boundary (Tatematsu et al. 1990; Uyaniker et al. 2003; Kothes et al. 2006; Gao et al. 2011a). Based on the $\Sigma - D$ relation, the distance of HB21 was estimated to be 1.0–1.6 kpc (Willis 1973; Clark & Caswell 1976; Caswell & Lerche 1979; Milne 1979). By observing the brightest stars in the Cyg OB complex with which HB21 is associated and assuming a maximum visual luminosity for red supergiants, Humphreys (1978) estimated the distance to be 800 ± 70 pc. Shan et al. (2018) got a distance of $1.9^{+0.3}_{-0.2}$ kpc based on RCs. Our estimation yields a distance being the largest since a conspicuous extinction jump occurs at 2.6 kpc. This is mainly because there are not so many tracers within 1.5–2.5 kpc. Additionally, the reddening profile derived from the dust map of Green et al. (2019) presents an increase of extinction from $\sim$2.0 kpc (see the corresponding subpanel in Figure 7). Thus, the distance of HB21 is suggested to be 2.3 kpc (mean value of 2.0–2.6 kpc) with an error of 0.3 kpc, in rough agreement with the Shan et al. (2018) result.
3. G93.7–0.2 is a shell-type SNR with some diffuse extensions (Gao et al. 2011a). Uyaniker et al. (2002) reported the neutral material around G93.7–0.2, and the H II region S124 in the lower left corner, which is visible in the corresponding subpanel of Figure 5. With the measurement of surrounding H II velocity and the standard Galactic rotation curve, Uyaniker et al. (2002) placed the SNR at a distance of 1.5 ± 0.2 kpc. Our fitting shows a farther distance at 2.16 ± 0.02 kpc. Foreground stars present a higher run of reddening than that of "*l*165." G93.7–0.2 is classified as Level A because of its conspicuous extinction jump and the dust grain radius consistent with an SNR, i.e., $\langle a \rangle_{sil} > \langle a \rangle_{gra}$.
4. G94.0+1.0. Foster & Routledge (2003) derived a distance–velocity relation with the H I 21 cm spectral line and used this relation to measure the distance to any object with a known systematic velocity. With this method, Foster (2005) suggested that G94.0+1.0 is expanding within a stellar wind bubble at a distance of 4.5 kpc. Many giant stars in our sample have apparently high extinctions in comparison with the reddening profile of "*l*165," which implies a distance <3 kpc. We suggest a distance of 2.53 kpc, with a relatively large uncertainty of 1.08 kpc. G94.0+1.0 was proposed to be a Perseus arm object (Foster 2005; Kothes et al. 2005), and thus, it should be closer than 3 kpc.
5. G109.1–1.0 (CTB 109). CTB 109 hosts an anomalous X-ray pulsar 1E 2259+586 (Koyama et al. 1989). With the H I observations, the distance of CTB 109 is determined as 3.0 kpc (Kothes et al. 2002) and 4.0 ± 0.8 kpc (Tian et al. 2010), respectively. Discrepantly, Durant & van Kerkwijk (2006) derived a much larger distance of $\sim$6 kpc with RC stars. In this study, there are not many sample stars toward G109.1–1.0, but they still lead to a reliable distance determination at 2.79 ± 0.04 kpc that is consistent with the kinematic estimate by Kothes et al. (2002).
6. G152.4–2.1 was identified as an SNR by Foster et al. (2013). Based on the H I emission and the Galactic rotation curve (Foster & Cooper 2010), the SNR is suggested to be within the Local arm at a distance of 1.1 ± 0.1 kpc. Our fitting results in a smaller distance at 0.59 ± 0.09 kpc. The discrepancy between the kinematic estimate and ours may be due to the application of an

undisturbed circular rotation curve (Foster et al. 2013), which would introduce considerable uncertainty for directions of Galactic anticenter like G152.4-2.1. On the other hand, Yu et al. (2019) suggested that G152.4-2.1 possibly associates with an MC located within 1.0 kpc, supporting our result. Meanwhile, the extinction jump around 1.5 kpc may refer to a background MC.

7. G156.2+5.7 is the first Galactic SNR discovered by strong X-ray emission (Pfeffermann et al. 1991). In the radio bands, the SNR displays a large shell structure with low surface brightness (Xu et al. 2007). Based on the Hα images and low resolution optical spectra, Gerardy & Fesen (2007) suggested there is physical interaction between G156.2+5.7 and a clump of interstellar clouds. According to the distances to these clouds, the SNR distance is suggested to be ~0.3 kpc. Other estimates are 1–3 kpc by the observation of associated H I emission (Reich et al. 1992); 1.3 kpc (Yamauchi et al. 1999) and 3 kpc (Pfeffermann et al. 1991) from the analysis of X-ray data. Both Pfeffermann et al. (1991) and Yamauchi et al. (1999) applied Sedov estimation to G156.2+5.7. The discrepancy (1.3 and 3 kpc) between their results is mainly caused by their different assumptions of the local environment based on the X-ray observations. Our sample stars bring about a reliable fitting toward G156.2+5.7, which indicates a distance of 0.68 kpc. The discrepancies between our result and the distances in literature are mainly due to the complex interstellar environments along this sightline. Tracers with high extinctions can be found from ~0.5 to $>$ 1.0 kpc.
8. G160.9+2.6 (HB9) is a large nearby SNR that has been mapped in multiple radio bands (Gao et al. 2011a). The distance to HB9 is determined by a small extinction jump at 0.54 kpc from our sample stars. It is consistent with 0.6 kpc by Yu et al. (2019) that proves the association of G160.9+2.6 with an MC. Considering the uncertainties, the measured distance is also consistent with the result of 0.8 ± 0.4 kpc based on the H I observations (Leahy & Tian 2007). A series of previous studies estimate the distance to be around 1 kpc, such as $\geqslant$1.1 kpc (Lozinskaya 1981), 1.1 kpc (Leahy 1987), and 1.3–1.8 kpc (Caswell & Lerche 1979). They show differences not only with ours but with others and with each other. These relatively old observations may suffer lower sensitivity and resultant larger uncertainties.
9. G166.0+4.3. The unusual shape of SNR G166.0+4.3, two shells with significantly different radii, caused a series of studies (see Kothes et al. 2006; Gao et al. 2011a), while the only credible estimate of its distance seems to be 4.5 ± 1.5 kpc by Landecker et al. (1989) based on the H I observation. We obtain two possible distances: 0.88 ± 0.01 kpc and 3.24 ± 0.03 kpc, respectively. The larger distance is favored and the closer jump is caused by some nearby cloud or the incompleteness of the tracers. An apparent jump of $E(g_{\rm P1} - K_{\rm S})$ can be seen for stars farther than 3 kpc, but there is no spatial separation for nearby and distant tracers. A distance of 3.24 kpc will make the SNR 240 pc above the Galactic plane, which is slightly larger than the typical scale-height of dust (Drimmel & Spergel 2001; Misiriotis et al. 2006).
10. G182.4+4.3. Kothes et al. (1998) identified G182.4+4.3, and reported a distance of $\geqslant$3 kpc by radio observations. But a tiny extinction jump indicates a distance of 1.05 ± 0.24 kpc that is consistent with the estimate (~1.1 kpc) based on the associated MC (Yu et al. 2019). It should be mentioned that the distance of Kothes et al. (1998) is very much model dependent. A possible cause is their underestimation of the ambient number density, i.e., a very small density of ISM ($0.013\,{\rm cm}^{-3}$), which leads the SNR to be very big and very far. While Yu et al. (2019) suggested that the SNR is associated with an MC so that the SNR is located in a dense medium and can sweep enough medium at much closer distance.
11. G189.1+3.0 (IC 443) is a well-known SNR located in a dense cloud (Troja et al. 2008), with distinct shells of various radii (Lee et al. 2008). A lot of studies are made on IC 443 throughout the whole spectrum, from gamma-ray to radio (e.g., Fesen 1984; Welsh & Sallmen 2003; Gao et al. 2011a; Acero et al. 2016; Koo et al. 2016; Planck Collaboration et al. 2016; Zhang et al. 2018). It interacts with the nearby MC, and the CO observation revealed a half molecular ring structure surrounding the SNR, from east to north (Su et al. 2014). An IR bright shell is also found in the northwest (Koo et al. 2016). 1.5 kpc is the most widely quoted distance to IC 443, assuming that the SNR interacts with the H II region S249 (Fesen & Kirshner 1980; Fesen 1984) whose distance is determined by the parallaxes of some stars from the Gem OB1 association (Cornett et al. 1977). This is confirmed by the empirical $\Sigma - D$ relation (Milne 1979; Caswell & Lerche 1979) and the SNR model (Chevalier 1999; Welsh & Sallmen 2003). From the optical systemic velocities, Lozinskaya (1981) placed IC 443 between 0.7 and 1.5 kpc. A recent study of the kinematics of the northeastern region of the SNR suggested a distance of 1.9 kpc (Ambrocio-Cruz et al. 2017). Our fitting yields a distance of 1.80 ± 0.05 with an apparent extinction jump, which is consistent with previous studies.
12. G190.9–2.2. Foster et al. (2013) first identified G190.9–2.2 as an SNR, with a barrel-shaped structure like G152.4–2.1. Based on the H I observation, Foster et al. (2013) put G190.9–2.3 at 1.0 kpc, with an uncertainty of 0.3 kpc. This result is consistent with our measurement 1.03 ± 0.01 kpc. The sharp increases of extinction at all 10 bands make the estimation very accurate. The shape of the fitted reddening profile is similar to G189.1+3.0 in that intense increase occurs behind the SNR.
13. G205.5+0.5 (Monoceros Nebula) is an old (1.5×10^5 yr Graham et al. 1982) SNR with fine filamentary structure (Davies 1963). The distance to Monoceros was estimated to be around 1.5 kpc by previous works (Davies et al. 1978; Graham et al. 1982; Leahy et al. 1986). In Paper I, we reported a distance of 1.98 kpc to Monoceros, and 1.55 kpc to the Rosette Nebula. As we discussed in Section 3.2, the distance of the Rosette Nebula is 1.58 kpc with the recently released data and the new method, which is consistent with Paper I. While for Monoceros, the present work yields two distances: 1.13 ± 0.01 kpc and 2.57 ± 0.02 kpc, respectively. The larger distance matches the position of the Perseus arm, while the small distance is consistent with the recent

determination by Yu et al. (2019) with the assumption that Monoceros interacts with neighboring MC. The large difference between present work and Paper I is mainly due to the methods used. In Paper I, we selected a reference region besides Monoceros to subtract the reddening contributed by foreground dust. The large dispersion of extinction from the reference regions shadowed the nearby extinction jump. Then, only the tracers around 1.98 kpc are outstanding. High-extinction tracers around 2.0 kpc can also be found in the corresponding subpanel in Figure 6. But our model preferred a more stable estimate, 2.57 kpc, for the second cloud rather than the distance of the closest tracers. Similar to the S147 SNR, the confusion of the Monoceros SNR case should at least partly be attributed to its low extinction due to its old age and, thus, thin dust shell.

The relation between the Monoceros SNR and the Rosette Nebula is widely debated. Davies et al. (1978) suggested that there is interaction between Monoceros and the Rosette Nebula, which is supported by Xiao & Zhu (2012) with the H I channel maps. Based on the optical, CO, and radio observations, Su et al. (2017) determined that the MCs at $V_{\rm LSR} \sim 5$ km s^{-1} and $\sim$19 km s^{-1} are both physically associated with Monoceros. As the Rosette Nebula is also surrounded by the 3–12 km s^{-1} and 18–23 km s^{-1} MCs, they suggested an association between Monoceros and the Rosette Nebula. Furthermore, based on the dust map of Green et al. (2015), a region centered at ($l = 204.^\circ107$, $b = 0.^\circ471$), the CO peak emission of the 5 km s^{-1} MCs, was selected to derive a distance of 1.6 kpc to the SNR which is consistent with the position of the Rosette Nebula. But an updated dust map of Green et al. (2019) indicates an extinction jump $<$1 kpc at ($l = 204.^\circ107$, $b = 0.^\circ471$) (see the corresponding subpanel in Figure 7) consistent with our estimation, while the Rosette Nebula is still kept at $\sim$1.6 kpc (the last subpanel in Figure 7). The Monoceros SNR is then $\sim$450 pc in front of the Rosette Nebula, so they hardly interact with each other. The associated MCs to Monoceros and Rosette Nebula may be located at different distances although they have similar velocities, for example, the MCs associated with NGC 2264 at about 900 pc also have $V_{\rm LSR} \sim 5$ km s^{-1} (Su et al. 2017).

14. G206.9+2.3. Davies et al. (1978) identified G206.9+2.3 as a distinct SNR from Monoceros based on optical observation. The SNR is very close to Monoceros and has a bright northwestern shell (Gao et al. 2011a). Graham et al. (1982) estimated a distance between 3–5 kpc by the $\Sigma - D$ relation. Assuming the SNR–MC association, Su et al. (2017) suggested a kinematic distance of 1.6 kpc to the SNR. We found the first conspicuous extinction jump at 0.89 $\pm$ 0.02 kpc. The second jump around 3.2 kpc is probably a fake feature because (1) not all the bands show a jump at this distance; (2) tracers with high extinctions farther than 1.0 kpc are generally on the same level, with no apparent jump after 3.0 kpc. Our estimate is much smaller than previous results. But we still classify G206.9+2.3 as Level A with the same reasons for G93.7–0.2. The low surface brightness of G206.9+2.3 and the early $\Sigma - D$ relation could introduce large uncertainty to the estimation of Graham et al. (1982). The difference between our result and that of Su et al. (2017) may be due to the uncertainty of the rotation curve toward the Galactic anticenter.
15. G213.0–0.6 is an old, shell-type SNR with extremely low radio surface brightness (Reich et al. 2003). Its association with the H II region S284 suggested a distance of 2.4 kpc (Stupar & Parker 2012). While Su et al. (2017) argued that there is no correlation between S284 and the SNR with the CO and radio observations, they obtained a kinematic distance of about 1.0 kpc. We infer an extinction jump at 1.09 $\pm$ 0.29 kpc. The very scattered distribution of tracers make the other tiny jump around 2.0 kpc unreliable.

A.2. Level B

1. G65.3+5.7 is a typical evolved shell-type SNR with very low surface brightness at λ6 cm and λ11 cm (Xiao et al. 2009). The referred region is bigger than the faint outline of the SNR seen in the radio map (Figure 5). But the stars inside the outlines are too few, so we take all of the sources in the reference region into account. Our model fitting yields two distance components at 1.51 kpc and 3.61 kpc, respectively. Considering the latitude of G65.3+5.7, a distance of 3.61 kpc means $\sim$360 pc above the Galactic plane, much larger than the typical scale-height around 100 pc of the dust disk (Drimmel & Spergel 2001; Misiriotis et al. 2006). Thus, we suggest that the distance to G65.3+5.7 is 1.51 $\pm$ 0.04 kpc, while the further extinction jump is caused by the incomplete tracers. Boumis et al. (2004) measured the expansion proper motion of the remnant's optical filamentary edge and a global expansion velocity of 155 km s^{-1}, which implied a distance of 0.77 $\pm$ 0.20 kpc. But this expansion velocity is much smaller than a few other measurements, which suggest a value of up to 400 km s^{-1}. Even with the lower limit of the velocity of 200 km s^{-1} given by Lozinskaia (1980), the distance should be larger than 0.99 kpc, in agreement with our estimation of 1.51 kpc if the error is taken into account. This case serves as an example to illustrate the uncertainty of the distance derived from the proper motion and shock velocity since both parameters can be quite uncertain. This SNR is classified as Level B because there are too few tracers and they are not in the central part.
2. G74.0–8.5 (the Cygnus Loop). G74.0–8.5 is a well-studied object in all observable bands, from X-ray (Koo et al. 2016) through optical (Blair et al. 2005) to radio (Sun et al. 2006). Minkowski (1958) calculated a kinematic distance of 770 pc. Blair et al. (2005) reported a distance of 540 pc to the Cygnus Loop, by measuring the proper motion and shock velocity with the *HST* data. Fesen et al. (2018) found three stars associated with the expanding shell of the Cygnus Loop remnant and determined its distance to be 735 $\pm$ 25 pc from the *Gaia* distances of these stars. In the region of the Cygnus Loop, we found many sample stars with relatively low extinction extending to over 6 kpc. Higher-extinction stars start to appear from 1 kpc and at any distance until 5 kpc. Limited by the number of the nearby sample stars, the model fitting yielded a null result on the distance, while a distance upper limit can be set at 1 kpc for the

Cygnus Loop because the higher-extinction stars start to appear from 1 kpc, and this is also consistent with all of the other estimates.

3. G82.2+5.3 (W63). Mavromatakis et al. (2004) made a multiwavelength study of G82.2+5.3 and suggested a distance between 1.6 and 3.3 kpc by the Sedov analysis. Rosado & Gonzalez (1981) suggested a distance of 1.6 kpc by measuring the expansion velocity of optical filaments. Our fitting results in a distance of 1.34 ± 0.13 kpc to W63, which is in line with these two estimates, while much smaller than the result of Shan et al. (2018), who probed a distance of 3.2 ± 0.4 kpc using RC stars. As W63 has not been verified to be associated with MCs and it has a comparatively similar $\langle a \rangle_{\rm gra}$ to $\langle a \rangle_{\rm sil}$, this case is classified as Level B.
4. G108.2–0.6 is first identified as a faint and large shell-type SNR by Tian et al. (2007). There are many bright objects around this SNR, such as SNR G109.1–1.0 (southeast), the bright H II region Sh2–142 (southwest), and the MC Sh2–152 (south). Based on the H I observations, Tian et al. (2007) suggested G108.2–0.6 is located in the Perseus arm, with a distance of 3.2 ± 0.6 kpc. Our analysis suggests a much smaller distance at 1.02 ± 0.01 kpc, which is well confined by many tracers with a strong extinction jump. The problem is the gap from ∼1.5 kpc to about 2.5 kpc: there are no tracers with high extinctions in this range, and the dwarfs are from the adjacent region rather than the SNR region. Furthermore, no associated MCs have been found. Thus, the measured object could be a foreground cloud, and finally G108.2–0.6 is classified as Level B.
5. G113.0+0.2 with strong polarized emission was discovered by Kothes et al. (2005), with the data of the Canadian Galactic Plane Survey. Kothes et al. (2005) determined the distance of G113.0+0.2 as 3.1 kpc through the observation of H I emission. Our result, <3.8 kpc, is consistent with it.
6. G116.9+0.2 (CTB 1). Fich (1986) suggested that G116.9 +0.2, G114.3+0.3, and G116.5+1.1 (for the latter two SNRs, see Appendix A.3) belong to the same group within a large H I shell in the Perseus arm, and the distance to CTB 1 is estimated to be 4.2 kpc. With the observational improvements and some additional constraints, Yar-Uyaniker et al. (2004) moved these three SNRs from the Perseus arm to the Local arm by determining their distances as 0.7 kpc for G114.3+0.3, 1.6 kpc for G116.5+1.1 and G116.9+0.2. Our analysis based on one cloud component yields an estimate of distance at 4.3 ± 0.2 kpc. If a two-component model is adopted, there will be a second component at around 1 kpc. It seems Fich (1986) and Yar-Uyaniker et al. (2004) detected the close and far components of our two-component model, respectively. The evidence to clarify which component is associated with the SNR is needed.
7. G127.1+0.5 is identified as a shell-type SNR by Caswell (1977) and Pauls (1977). Several compact sources are near the center (Kaplan et al. 2004), and there is a fairly circular shell from north to northeast (Sun et al. 2007). Zhou et al. (2014) discovered a pre-existing molecular filament from the CO observation with which G127.1 +0.5 is associated. This association implies a distance of ∼300 pc. The possible association of the SNR with NGC 559 (Rose & Hintz 2007) and an H I bubble (Leahy & Tian 2006) sets a distance of 1.3 kpc (Zhou et al. 2014). Meanwhile, Leahy & Tian (2006) suggested its distance to be 1.15 kpc within an upper limit of 2.9 kpc. Our sample stars set an upper limit at about 2.9 kpc, highly consistent with Leahy & Tian (2006).

A.3. Level C

1. G65.1+0.6 is a faint shell-type SNR with strong southern emission (Landecker et al. 1990). Based on the associated H I observations, Tian & Leahy (2006) proposed a rather large distance of 9.2 kpc. Our fitting shows a distance of 1.33 kpc. Since there are not enough tracers between 1.0 and 2.5 kpc, the distance uncertainty may be up to 0.6 kpc. It should be noted that there are no tracers farther than 7 kpc due to the sensitivity limit of the spectroscopic surveys; consequently, the extinction jump at a distance like 9.2 kpc would not show up, and the present detection of the jump at 1 kpc might be caused by a local foreground MC. The large discrepancy between our result and the kinematic estimate places this case into Level C. Meanwhile, there are no other reliable studies about its distance and the association with MCs.
2. G67.6+0.9 was discovered by Sabin et al. (2013). Shan et al. (2018) probed a distance of 3.2 ± 0.4 kpc by RC stars. There are five tracers toward G67.6+0.9, and all of them exhibit much larger extinctions than "l165." So the distance upper limit is defined as the location of the nearest tracer, i.e., 2.6 kpc although, it is still much smaller than the distance derived from the RC stars.
3. G70.0–21.5 and G159.6+7.3. Both are identified as SNRs by the numerous optical filaments from the VTSS Hα images (Fesen & Milisavljevic 2010; Fesen et al. 2015). But the available radio observations for G70.0–21.5 (GB6S λ6 cm) and G159.6+7.3 (WENSS 325 MHz) show no SNR-like structures. Our tracers neither exhibit any apparent extinction jump. The runs of reddening toward them after 1.0 kpc are very flat, implying the deviation from the Galactic dust disk. Based on a shock velocity estimate, Fesen et al. (2015) derived a distance of 1–2 kpc to G70.0–21.5. While for G159.6+7.3, no distance information is available. No reliable estimation can be made by our star sample.
4. G114.3+0.3 and G116.5+1.1. Reich & Braunsfurth (1981) discovered G114.3+0.3 and G116.5+1.1, and they suggested their distance as 3.4 kpc and 3.6–5.2 kpc, respectively, based on the velocity of the possibly associated H I region. Fich (1986) suggested that these two SNRs, plus G116.9+0.2, belong to the same group within a large H I shell in the Perseus arm, with a distance of 4.2 kpc. With the observational improvements and some additional constraints including the optical emission (Fesen et al. 1997) and the polarization horizon (Uyaniker et al. 2003), Yar-Uyaniker et al. (2004) moved these three SNRs from the Perseus arm to the Local arm after determining their distances as 0.7 kpc for G114.3+0.3, 1.6 kpc for G116.5+1.1 and G116.9+0.2. Our data set a distance upper limit of G114.3+0.3 to be 2.7 kpc. Most of the tracers of G116.5+1.1 are farther than 3.0 kpc, while the nearest one indicates a distance of 0.68 kpc, which is consistent with the distance derived from the 3D

dust map (see Section 4.1.1). So, G116.5+1.1 is suggested to be located either at 0.68 kpc or within 3.0 kpc. The estimates to both of these two SNRs are consistent with the results of Yar-Uyaniker et al. (2004). In Appendix A.2, G116.9+0.2 is determined as far as 4.3 ± 0.2 kpc, consistent with Reich & Braunsfurth (1981) while farther than Yar-Uyaniker et al. (2004). Our results provide the possibility that these three SNRs are located in the Perseus arm. But because no foreground tracers are available, we cannot exclude the possibility that G114.3+0.3 and G116.5+1.1 may be located in the Local arm.

5. G119.5+10.2 (CTA 1), discovered by Harris & Roberts (1960), is a composite SNR, with semi-circular shell and strong optical filaments (Sun et al. 2011). H I observations are used to derive a distance of 1.4 ± 0.3 kpc (Pineault et al. 1993). Our tracers present a flat reddening profile with almost no increase of extinction to a distant zone. Thus, no reliable estimate can be made.
6. G178.2–4.2. Gao et al. (2011b) identified this SNR and studied its radio properties. No H I cavity is detected toward the sightline of G178.2–4.2. Neither the $\Sigma - D$ relation can yield a reasonable distance (Gao et al. 2011b). High-extinction tracers in our sample have a wide distribution in distance from 0.3 to 5 kpc, but there is no apparent extinction jump along the distance. Consequently, the distance to G178.2–4.2 cannot be well determined, and we suggest that this SNR is located within 0.3 kpc or farther than 5 kpc.
7. G179.0+2.6 was first identified as a thick shell-type SNR by Fuerst & Reich (1986). The SNR exhibits coincident optical emission consisting of diffuse filamentary features (How et al. 2018). The distance measurement based on the $\Sigma - D$ relation is very uncertain in a wide range: 3.5 kpc (Fuerst & Reich 1986), 6.1 kpc (Case & Bhattacharya 1998), 2.9 kpc (Guseinov et al. 2003), and 3.1 kpc (Pavlovic et al. 2014). From our sample, a few tracers with high extinctions are farther than 3 kpc, but our model determines its distance at 0.92 ± 0.04 kpc with a relatively small extinction jump (see Figure 6). The tracers around 2 kpc with $E(g_{\rm P1} - K_{\rm S}) > 1.0$ mag smoothen the increase of extinction from nearby to over 3 kpc so that the jump at 0.92 kpc becomes significant. As a result, the tiny extinction jump may only indicate a foreground MC.
8. G180.0–1.7 (S147) is one of the most famous evolved SNRs in the Milky Way, with beautiful filaments in optical bands. It was first identified as an SNR by Minkowski (1958). A lot of studies on the distance to S147 have been done. Based on $\Sigma - D$ relation, the distances are 0.8–1.37 kpc (Kundu et al. 1980), 0.9 kpc (Clark & Caswell 1976), 1.06 kpc (Guseinov et al. 2003), and 1.6 ± 0.3 kpc (Sofue et al. 1980). The dispersion is mainly due to the differences in models and observational data. By measuring the distance to the pulsar located in S147, three consistent results are obtained: 1.2 kpc (Kramer et al. 2003), $1.47^{+0.42}_{-0.27}$ kpc (Ng et al. 2007), and $1.3^{+0.22}_{-0.16}$ kpc (Chatterjee et al. 2009). Based on the detection of the pre-supernova binary companion HD 37424, Dinçel et al. (2015) suggested a distance of $1.333^{+0.103}_{-0.112}$ kpc. Using multiband photometric data from the Xuyi Schmidt Telescope Photometric Survey of the Galactic Anticentre (XSTPS-GAC), 2MASS, and *WISE*, Chen et al. (2017) investigated some dense regions in S147, and obtained a distance of 1.22 ± 0.21 kpc. All of these derived distances are around 1.2 kpc. Our model yields two clouds at the distances of 0.38 ± 0.10 kpc and 2.51 ± 0.78 kpc, respectively, neither of which agrees with previous consensus at 1.2 kpc. From Figure 6, it can be seen that the smaller distance suffers large uncertainty and may trace a foreground cloud that is also reported by Chen et al. (2017). The larger distance is probably caused by the Perseus arm. Nevertheless, many stars with high extinction ($E(g_{\rm P1} - K_{\rm S}) > 1.0$ mag) are widely distributed between ~0.2−1.5 kpc and located in the whole western part of S147. It seems that our extinction-distance model is not able to clearly peel S147 from the foreground cloud, which exposes the inability of our method to the old SNRs with weak extinction.

ORCID iDs

He Zhao https://orcid.org/0000-0003-2645-6869
Biwei Jiang https://orcid.org/0000-0003-3168-2617

References

Abolfathi, B., Aguado, D. S., Aguilar, G., et al. 2018, ApJS, 235, 42
Acero, F., Ackermann, M., Ajello, M., et al. 2016, ApJS, 224, 8
Ambrocio-Cruz, P., Rosado, M., de la Fuente, E., Silva, R., & Blanco-Piñon, A. 2017, MNRAS, 472, 51
Andersen, M., Rho, J., Reach, W. T., Hewitt, J. W., & Bernard, J. P. 2011, ApJ, 742, 7
Anguiano, B., Majewski, S. R., Allende-Prieto, C., et al. 2018, A&A, 620, A76
Arendt, R. G., Dwek, E., & Moseley, S. H. 1999, ApJ, 521, 234
Astropy Collaboration, Robitaille, T. P., Tollerud, E. J., et al. 2013, A&A, 558, A33
Bailer-Jones, C. A. L., Rybizki, J., Fouesneau, M., Mantelet, G., & Andrae, R. 2018, AJ, 156, 58
Bevan, A., Barlow, M. J., & Milisavljevic, D. 2017, MNRAS, 465, 4044
Blair, W. P., Sankrit, R., & Raymond, J. C. 2005, AJ, 129, 2268
Boumis, P., Meaburn, J., López, J. A., et al. 2004, A&A, 424, 583
Cardelli, J. A., Clayton, G. C., & Mathis, J. S. 1989, ApJ, 345, 245
Case, G. L., & Bhattacharya, D. 1998, ApJ, 504, 761
Caswell, J. L. 1977, MNRAS, 181, 789
Caswell, J. L., & Lerche, I. 1979, MNRAS, 187, 201
Chatterjee, S., Brisken, W. F., Vlemmings, W. H. T., et al. 2009, ApJ, 698, 250
Chen, B. Q., Huang, Y., Yuan, H. B., et al. 2019, MNRAS, 483, 4277
Chen, B.-Q., Liu, X.-W., Ren, J.-J., et al. 2017, MNRAS, 472, 3924
Chevalier, R. A. 1999, ApJ, 511, 798
Churchwell, E., Babler, B. L., Meade, M. R., et al. 2009, PASP, 121, 213
Clark, D. H., & Caswell, J. L. 1976, MNRAS, 174, 267
Cohen, M., Wheaton, W. A., & Megeath, S. T. 2003, AJ, 126, 1090
Condon, J. J., Broderick, J. J., & Seielstad, G. A. 1991, AJ, 102, 2041
Condon, J. J., Broderick, J. J., Seielstad, G. A., Douglas, K., & Gregory, P. C. 1994, AJ, 107, 1829
Cornett, R. H., Chin, G., & Knapp, G. R. 1977, A&A, 54, 889
Cutri, R. M., Skrutskie, M. F., van Dyk, S., et al. 2003, The IRSA 2MASS All-Sky Point Source Catalog, http://irsa.ipac.caltech.edu/applications/Gator/
Dame, T. M., Hartmann, D., & Thaddeus, P. 2001, ApJ, 547, 792
Davies, R. D. 1963, Obs, 83, 172
Davies, R. D., Elliott, K. H., Goudis, C., Meaburn, J., & Tebbutt, N. J. 1978, A&AS, 31, 271
Deng, L. 2014, in IAU Symp. 298, Setting the Scene for Gaia and LAMOST, ed. S. Feltzing et al. (Cambridge: Cambridge Univ. Press), 269
Dinçel, B., Neuhäuser, R., Yerli, S. K., et al. 2015, MNRAS, 448, 3196
Draine, B. T. 2003, ARA&A, 41, 241
Draine, B. T. 2009, in ASP Conf. Ser. 414, Interstellar Dust Models and Evolutionary Implications, ed. T. Henning, E. Grün, & J. Steinacker (San Francisco, CA: ASP), 453
Draine, B. T. 2011, Physics of the Interstellar and Intergalactic Medium (Princeton, NJ: Princeton Univ. Press)
Drimmel, R., & Spergel, D. N. 2001, ApJ, 556, 181

Ducati, J. R., Bevilacqua, C. M., Rembold, S. B., & Ribeiro, D. 2001, ApJ, 558, 309
Durant, M., & van Kerkwijk, M. H. 2006, ApJ, 650, 1070
Dwek, E., Foster, S. M., & Vancura, O. 1996, ApJ, 457, 244
Eisenstein, D. J., Weinberg, D. H., Agol, E., et al. 2011, AJ, 142, 72
Fesen, R. A. 1984, ApJ, 281, 658
Fesen, R. A., & Kirshner, R. P. 1980, ApJ, 242, 1023
Fesen, R. A., & Milisavljevic, D. 2010, AJ, 140, 1163
Fesen, R. A., Neustadt, J. M. M., Black, C. S., & Koeppel, A. H. D. 2015, ApJ, 812, 37
Fesen, R. A., Weil, K. E., Cisneros, I. A., Blair, W. P., & Raymond, J. C. 2018, MNRAS, 481, 1786
Fesen, R. A., Winkler, F., Rathore, Y., et al. 1997, AJ, 113, 767
Fich, M. 1986, ApJ, 303, 465
Foreman-Mackey, D., Hogg, D. W., Lang, D., & Goodman, J. 2013, PASP, 125, 306
Foster, T. 2005, A&A, 441, 1043
Foster, T., & Cooper, B. 2010, in ASP Conf. Ser. 438, The Dynamic Interstellar Medium: A Celebration of the Canadian Galactic Plane Survey, ed. R. Kothes, T. L. Landecker, & A. G. Willis (San Francisco, CA: ASP), 16
Foster, T., & Routledge, D. 2003, ApJ, 598, 1005
Foster, T. J., Cooper, B., Reich, W., Kothes, R., & West, J. 2013, A&A, 549, A107
Fuerst, E., & Reich, W. 1986, A&A, 154, 303
Gaia Collaboration, Brown, A. G. A., Vallenari, A., et al. 2018, A&A, 616, A1
Gao, X. Y., Han, J. L., Reich, W., et al. 2011a, A&A, 529, A159
Gao, X. Y., Reich, W., Han, J. L., et al. 2010, A&A, 515, A64
Gao, X. Y., Sun, X. H., Han, J. L., et al. 2011b, A&A, 532, A144
Gerardy, C. L., & Fesen, R. A. 2007, MNRAS, 376, 929
Graham, D. A., Haslam, C. G. T., Salter, C. J., & Wilson, W. E. 1982, A&A, 109, 145
Green, D. A. 2019, JApA, 40, 36
Green, G. M., Schlafly, E., Zucker, C., Speagle, J. S., & Finkbeiner, D. 2019, ApJ, 887, 93
Green, G. M., Schlafly, E. F., Finkbeiner, D. P., et al. 2015, ApJ, 810, 25
Guillet, V., Jones, A. P., & Pineau Des Forêts, G. 2009, A&A, 497, 145
Guseinov, O. H., Ankay, A., Sezer, A., & Tagieva, S. O. 2003, A&AT, 22, 273
Hanbury Brown, R., & Hazard, C. 1953, MNRAS, 113, 123
Harris, D. E., & Roberts, J. A. 1960, PASP, 72, 237
Henden, A., & Munari, U. 2014, CoSka, 43, 518
Henden, A. A., Templeton, M., Terrell, D., et al. 2016, VizieR On-line Data Catalog, II/336
Hodapp, K. W., Kaiser, N., Aussel, H., et al. 2004, AN, 325, 636
How, T. G., Fesen, R. A., Neustadt, J. M. M., Black, C. S., & Outters, N. 2018, MNRAS, 478, 1987
Humphreys, R. M. 1978, ApJS, 38, 309
Jian, M., Gao, S., Zhao, H., & Jiang, B. 2017, AJ, 153, 5
Jiang, B., Chen, Y., Wang, J., et al. 2010, ApJ, 712, 1147
Jones, A. P., Tielens, A. G. G. M., Hollenbach, D. J., & McKee, C. F. 1994, ApJ, 433, 797
Jordi, C., Gebran, M., Carrasco, J. M., et al. 2010, A&A, 523, A48
Kaplan, D. L., Frail, D. A., Gaensler, B. M., et al. 2004, ApJS, 153, 269
Koo, B.-C., Lee, J.-J., Jeong, I.-G., Seok, J. Y., & Kim, H.-J. 2016, ApJ, 821, 20
Kos, J. 2017, MNRAS, 468, 4255
Kothes, R., Fedotov, K., Foster, T. J., & Uyanıker, B. 2006, A&A, 457, 1081
Kothes, R., Furst, E., & Reich, W. 1998, A&A, 331, 661
Kothes, R., Uyanıker, B., & Reid, R. I. 2005, A&A, 444, 871
Kothes, R., Uyaniker, B., & Yar, A. 2002, ApJ, 576, 169
Koyama, K., Nagase, F., Ogawara, Y., et al. 1989, PASJ, 41, 461
Kramer, M., Lyne, A. G., Hobbs, G., et al. 2003, ApJL, 593, L31
Kundu, M. R., Angerhofer, P. E., Fuerst, E., & Hirth, W. 1980, A&A, 92, 225
Lakićević, M., van Loon, J. T., Meixner, M., et al. 2015, ApJ, 799, 50
Landecker, T. L., Clutton-Brock, M., & Purton, C. R. 1990, A&A, 232, 207
Landecker, T. L., Pineault, S., Routledge, D., & Vaneldik, J. F. 1989, MNRAS, 237, 277
Landecker, T. L., Roger, R. S., & Higgs, L. A. 1980, A&AS, 39, 133
Leahy, D., & Tian, W. 2006, A&A, 451, 251
Leahy, D. A. 1987, ApJ, 322, 917
Leahy, D. A., Green, K., & Ranasinghe, S. 2013, MNRAS, 436, 968
Leahy, D. A., Naranan, S., & Singh, K. P. 1986, MNRAS, 220, 501
Leahy, D. A., & Tian, W. W. 2007, A&A, 461, 1013
Lee, J.-J., Koo, B.-C., Yun, M. S., et al. 2008, AJ, 135, 796
Lozinskaia, T. A. 1980, A&A, 84, 26
Lozinskaya, T. A. 1981, SvAL, 7, 29
Majewski, S. R. & APOGEE Team 2016, AN, 337, 863
Mathis, J. S., Rumpl, W., & Nordsieck, K. H. 1977, ApJ, 217, 425
Matsuura, M., Dwek, E., Barlow, M. J., et al. 2015, ApJ, 800, 50
Mavromatakis, F., Aschenbach, B., Boumis, P., & Papamastorakis, J. 2004, A&A, 415, 1051
Milne, D. K. 1979, AuJPh, 32, 83
Minkowski, R. 1958, RvMP, 30, 1048
Misiriotis, A., Xilouris, E. M., Papamastorakis, J., Boumis, P., & Goudis, C. D. 2006, A&A, 459, 113
Munari, U., Henden, A., Frigo, A., et al. 2014, AJ, 148, 81
Ng, C.-Y., Romani, R. W., Brisken, W. F., Chatterjee, S., & Kramer, M. 2007, ApJ, 654, 487
Nozawa, T., Kozasa, T., Habe, A., et al. 2007, ApJ, 666, 955
Onaka, P., Tonry, J. L., Isani, S., et al. 2008, Proc. SPIE, 7014, 70140D
Owen, P. J., & Barlow, M. J. 2015, ApJ, 801, 141
Pauls, T. 1977, A&A, 59, L13
Pavlovic, M. Z., Dobardzic, A., Vukotic, B., & Urosevic, D. 2014, SerAJ, 189, 25
Pfeffermann, E., Aschenbach, B., & Predehl, P. 1991, A&A, 246, L28
Pineault, S., Landecker, T. L., Madore, B., & Gaumont-Guay, S. 1993, AJ, 105, 1060
Planck Collaboration, Arnaud, M., Ashdown, M., et al. 2016, A&A, 586, A134
Reich, P., Reich, W., & Furst, E. 1997, A&AS, 126, 413
Reich, W., & Braunsfurth, E. 1981, A&A, 99, 17
Reich, W., Fuerst, E., & Arnal, E. M. 1992, A&A, 256, 214
Reich, W., Reich, P., & Fuerst, E. 1990, A&AS, 83, 539
Reich, W., Zhang, X., & Fürst, E. 2003, A&A, 408, 961
Rengelink, R. B., Tang, Y., de Bruyn, A. G., et al. 1997, A&AS, 124, 259
Rho, J., Kozasa, T., Reach, W. T., et al. 2008, ApJ, 673, 271
Rosado, M., & Gonzalez, J. 1981, RMxAA, 5, 93
Rose, M. B., & Hintz, E. G. 2007, AJ, 134, 2067
Sabin, L., Parker, Q. A., Contreras, M. E., et al. 2013, MNRAS, 431, 279
Schlafly, E. F., & Finkbeiner, D. P. 2011, ApJ, 737, 103
Schlafly, E. F., Finkbeiner, D. P., Jurić, M., et al. 2012, ApJ, 756, 158
Schlafly, E. F., Meisner, A. M., Stutz, A. M., et al. 2016, ApJ, 821, 78
Shan, S. S., Zhu, H., Tian, W. W., et al. 2018, ApJS, 238, 35
Sofue, Y., Furst, E., & Hirth, W. 1980, PASJ, 32, 1
Stupar, M., & Parker, Q. A. 2012, MNRAS, 419, 1413
Su, Y., Fang, M., Yang, J., Zhou, P., & Chen, Y. 2014, ApJ, 788, 122
Su, Y., Zhou, X., Yang, J., et al. 2017, ApJ, 836, 211
Sun, X. H., Han, J. L., Reich, W., et al. 2007, A&A, 463, 993
Sun, X. H., Reich, W., Han, J. L., Reich, P., & Wielebinski, R. 2006, A&A, 447, 937
Sun, X. H., Reich, W., Wang, C., Han, J. L., & Reich, P. 2011, A&A, 535, A64
Tatematsu, K., Fukui, Y., Landecker, T. L., & Roger, R. S. 1990, A&A, 237, 189
Temim, T., & Dwek, E. 2013, ApJ, 774, 8
Temim, T., Slane, P., Arendt, R. G., & Dwek, E. 2012, ApJ, 745, 46
Tian, W. W., & Leahy, D. A. 2006, A&A, 455, 1053
Tian, W. W., & Leahy, D. A. 2012, MNRAS, 421, 2593
Tian, W. W., Leahy, D. A., & Foster, T. J. 2007, A&A, 465, 907
Tian, W. W., Leahy, D. A., & Li, D. 2010, MNRAS, 404, L1
Tonry, J. L., Stubbs, C. W., Lykke, K. R., et al. 2012, ApJ, 750, 99
Troja, E., Bocchino, F., Miceli, M., & Reale, F. 2008, A&A, 485, 777
Uyaniker, B., Fürst, E., Reich, W., Reich, P., & Wielebinski, R. 1999, A&AS, 138, 31
Uyaniker, B., Kothes, R., & Brunt, C. M. 2002, ApJ, 565, 1022
Uyaniker, B., Landecker, T. L., Gray, A. D., & Kothes, R. 2003, ApJ, 585, 785
Wang, S., & Chen, X. 2019, ApJ, 877, 116
Wang, S., & Jiang, B. W. 2014, ApJL, 788, L12
Wang, S., Jiang, B. W., Zhao, H., Chen, X., & de Grijs, R. 2017, ApJ, 848, 106
Weingartner, J. C., & Draine, B. T. 2001, ApJ, 548, 296
Welsh, B. Y., & Sallmen, S. 2003, A&A, 408, 545
Willis, A. G. 1973, A&A, 26, 237
Wright, E. L., Eisenhardt, P. R. M., Mainzer, A. K., et al. 2010, AJ, 140, 1868
Xiao, L., Reich, W., Fürst, E., & Han, J. L. 2009, A&A, 503, 827
Xiao, L., & Zhu, M. 2012, A&A, 545, A86
Xu, J. W., Han, J. L., Sun, X. H., et al. 2007, A&A, 470, 969
Xue, M., Jiang, B. W., Gao, J., et al. 2016, ApJS, 224, 23
Yamauchi, S., Koyama, K., Tomida, H., Yokogawa, J., & Tamura, K. 1999, PASJ, 51, 13
Yar-Uyaniker, A., Uyaniker, B., & Kothes, R. 2004, ApJ, 616, 247
Yu, B., Chen, B. Q., Jiang, B. W., & Zijlstra, A. 2019, MNRAS, 488, 3129
Zhang, S., Tang, X., Zhang, X., et al. 2018, ApJ, 859, 141
Zhao, G., Zhao, Y.-H., Chu, Y.-Q., Jing, Y.-P., & Deng, L.-C. 2012, RAA, 12, 723
Zhao, H., Jiang, B., Gao, S., Li, J., & Sun, M. 2018, ApJ, 855, 12
Zhou, X., Yang, J., Fang, M., & Su, Y. 2014, ApJ, 791, 109